Pacific Northwest
NATIONAL LABORATORY

PNNL-39169, Rev. 0
ITSW-RPT-011, Rev. 0

Project Year 2 Task 4: Studies of Phosphate and Fluoride Solubility for Dissolution of High Phosphate Tank Waste

March 2026

Trent R. Graham, Ashley Kennedy, Winnie Liu, Ege Uyar, Daria V. Boglaienko, Aidan C. Henson, Jacob I. Morton, Stony T. Akins, Abdullah Ozkanlar, Mark E. Bowden, Aurora E. Clark, Hsiu-Wen Wang, Reid A. Peterson, and Carolyn I. Pearce

U.S. DEPARTMENT of ENERGY

Prepared for the U.S. Department of Energy
under Contract DE-AC05-76RL01830

DISCLAIMER

PACIFIC NORTHWEST NATIONAL LABORATORY
operated by
BATTELLE
for the
UNITED STATES DEPARTMENT OF ENERGY
under Contract DE-AC05-76RL01830

Printed in the United States of America

Available to DOE and DOE contractors from the
Office of Scientific and Technical Information,
P.O. Box 62, Oak Ridge, TN 37831-0062;
ph: (865) 576-8401
fax: (865) 576-5728
email: reports@adonis.osti.gov

Available to the public from the National Technical Information Service
5301 Shawnee Rd., Alexandria, VA 22312
ph: (800) 553-NTIS (6847)
email: orders@ntis.gov <https://www.ntis.gov/about>
Online ordering: http://www.ntis.gov

PNNL-39169, Rev. 0
ITSW-RPT-011, Rev. 0

Project Year 2 Task 4: Studies of Phosphate and Fluoride Solubility for Dissolution of High Phosphate Tank Waste

March 2026

Trent R. Graham, Ashley Kennedy, Winnie Liu, Ege Uyar, Daria V. Boglaienko, Aidan C. Henson, Jacob I. Morton, Stony T. Akins, Abdullah Ozkanlar, Mark E. Bowden, Aurora E. Clark, Hsiu-Wen Wang, Reid A. Peterson, and Carolyn I. Pearce

Prepared for
the U.S. Department of Energy
under Contract DE-AC05-76RL01830

Pacific Northwest National Laboratory
Richland, Washington 99354

Summary

The goal of this work is to accelerate waste retrieval at the Hanford Site by enabling delivery of high-level waste sludge to the Waste Treatment and Immobilization Plant through in-tank processing in the southeast (SE) quadrant of the Hanford tank farms. There is a significant amount of insoluble phosphate and fluoride in SE quadrant tank waste in the form of natrophosphate ($Na_7F(PO_4)_2 \cdot 19H_2O$). Solubility studies of natrophosphate and other tank waste materials [gibbsite, ($Al(OH)_3$) and trisodium phosphate (Na_3PO_4)] in the complex tank waste matrix that contains sodium salts of hydroxide (OH^-), phosphate (PO_4^{3-}), fluoride (F^-), nitrate (NO_3^-), nitrite (NO_2^-), and aluminate ($Al(OH)_4^-$) are limited. Project 82521 Task 4 is addressing these knowledge gaps by conducting solubility tests with sodium phosphate, natrophosphate, and gibbsite in simulant solutions relevant to in-tank processing. The simulants are simple 3.8 M sodium (Na) solutions and complex multicomponent 3.8 M simulant solutions based on high natrophosphate segments in tanks AN-101 and AN-106.

Solubility studies in Project Year 1 revealed that PO_4^{3-} solubility was higher in mixed NO_3^- and carbonate (CO_3^{2-}) solutions than in solutions containing OH^-, at a fixed Na concentration of 3.8 M. Therefore, simulant solutions with variable CO_3^{2-}, OH^-, and NO_3^- concentrations were used in project Year 2 to evaluate the effects of total Na, OH^-, and CO_3^{2-} on PO_4^{3-} solubility. The relative effects of CO_3^{2-} vs. OH^- on total PO_4^{3-} solubility were the same with variable Na concentrations. These results show that changes to PO_4^{3-} solubility upon addition of $OH^-$and CO_3^{2-} do not scale with alkalinity and that electrolyte identity influences PO_4^{3-} solubility when sodium is not fixed.

Solubility studies were also conducted with trisodium phosphate dodecahydrate to investigate the potential influence of co-dissolution of fluoride with phosphate in the natrophosphate tests. As with natrophosphate, hydroxide decreased phosphate solubility the most, mixtures of hydroxide and carbonate were intermediate, and carbonate decreased phosphate solubility the least. These results confirm that the effect of carbonate and hydroxide addition on phosphate solubility is not related to phosphate-fluoride coupling but instead reflects broader alkalinity partitioning effects.

Increasing carbonate concentration in a multicomponent 3.8 M sodium simulant did not induce precipitation of dissolved phosphate. Increasing hydroxide concentration resulted in a concurrent decrease in phosphate solubility, showing the same trend as in the simple solutions. In tests containing both natrophosphate and gibbsite, consumption of hydroxide through aluminum dissolution stabilized phosphate concentrations in solution. Subsequent dilution of the simulant after natrophosphate and gibbsite dissolution did not result in precipitation of phosphate or aluminum, indicating stability under operationally relevant conditions.

Collectively, these results demonstrate that phosphate solubility in concentrated alkaline sodium systems is governed jointly by sodium activity and alkalinity partitioning. Elevated sodium decreases solubility, while electrolyte identity, specifically the distribution of alkalinity between hydroxide and carbonate, determines the extent to which phosphate solubility is affected.

Acknowledgments

The authors would like to thank Dr. Ming Zhu (DOE Office of Environmental Management) and the Lab Policy Office for supporting this work. The authors also thank Renee Russell for her independent technical review of this report. The authors are extremely grateful to analytical chemists Teresa Lemmon and Marie Swita for solution phase analysis at the PNNL Bioscience and Engineering Laboratory Analytical Lab as part of the Chemical and Biological Processing Group in the Energy and Environment Directorate at PNNL. The authors also thank Jackie Hager and Nancy Escobedo for the quality review of the data package, David MacPherson for his review of this report, and Matthew Wilburn for his technical editing. Graduate Fellows Ashley Kennedy and Jacob Morton were supported by the DOE Office of Environmental Management's Minority Serving Institutions Partnership Program. PNNL is operated by Battelle for the U.S. Department of Energy under the contract DE-AC05-76RL01830.

Acronyms and Abbreviations

AIMD	*ab initio* molecular dynamics
BAR	Bennett acceptance ratio
BBI	best basis inventory
DI	deionized
FID	free induction decay
FY	fiscal year
HLW	high-level waste
IC	ion chromatography
ICP-OES	inductively coupled plasma-optical emission spectroscopy
LAW	low-activity waste
LJ	Lennard-Jones
NA	not applicable
NMR	nuclear magnetic resonance
NPT	isothermal–isobaric ensemble (constant number of particles, pressure, and temperature)
NQAP	Nuclear Quality Assurance Program
PFG	pulsed-field gradient
PNNL	Pacific Northwest National Laboratory
RPL	Radiochemical Processing Laboratory
SST	single-shell tank
TIC	total inorganic carbon
TSPD	trisodium phosphate dodecahydrate
vdW	van der Waals
WTP	Waste Treatment and Immobilization Plant

Contents

Summary iii
Acknowledgments iv
Acronyms and Abbreviations v
1.0 Introduction 1
2.0 Quality Assurance 2
3.0 Materials and Methods 3
3.1 Reagents 3
3.2 Gibbsite Synthesis 3
3.3 Natrophosphate Synthesis 3
3.4 Simulant Preparation 3
3.5 Apparatus for Solubility Experiments 4
3.6 Sampling Solubility Experiments 4
3.7 Solution Phase Analysis 5
3.8 Variable Temperature Raman Spectroscopy 5
3.9 Variable Temperature PFG-NMR Spectroscopy 5
3.10 X-ray Diffraction 6
3.11 Simulations 6
3.11.1 Simulation Details 6
3.11.2 Radial Distribution Functions 7
3.11.3 Diffusion Coefficients 8
3.11.4 Umbrella Sampling Simulations 8
3.11.5 Water Activities 8
3.11.6 Solid Simulations 9
3.11.7 Solid-Liquid Interfacial Systems 10
3.11.8 Phosphate Systems with Fluoride 11
4.0 Solubility Results 12
4.1 Trisodium Phosphate Dodecahydrate Solubility in Solutions with Varying Sodium Concentration 12
4.1.1 Solution Phase Data 12
4.1.2 Solid Phase Characterization 14
4.1.3 Physicochemical Characterization 15
4.2 Natrophosphate Solubility in Solutions with Fixed Total Sodium Concentration (3.8 M) 16
4.2.1 Solution Phase Data 16
4.2.2 Solid Phase Characterization 19
4.2.3 Incongruent Natrophosphate Dissolution 19
4.2.4 Physicochemical Characterization 20

4.3 Natrophosphate Solubility in Solutions with Varying Na Concentration 20
4.3.1 Solution Phase Data 20
4.3.2 Solid State Characterization 22
4.3.3 Incongruent Natrophosphate Dissolution 22
4.3.4 Physicochemical Characterization 22
4.4 Carbonate Solubility in a 3.8 M Na Multicomponent Simulant 23
4.4.1 Solution Phase Data 23
4.4.2 Solid Phase Characterization 24
4.4.3 Physicochemical Characterization 25
4.5 Phosphorus and Aluminum Solubility in Coupled Gibbsite–Natrophosphate Systems 25
4.5.1 Solution Phase Studies 25
4.5.2 Solid Phase Characterization 27
4.5.3 Physicochemical Characterization 28
4.5.4 Effect of Dilution on Phosphate and Aluminum Solubility 28
5.0 Computational Chemistry Results 30
5.1 Development of a New Force Field for Alkaline Phosphate Solutions 30
5.2 Concentration-Dependent Aggregation Behavior of Na_3PO_4 32
5.3 Solid-Liquid Interfacial Chemistry of Na_3PO_4 Polymorphs 36
6.0 Extension to Real Hanford Tank Waste 38
6.1 Aluminum Solubility 38
6.2 Phosphate and Fluoride Solubility 39
7.0 Conclusions 41
8.0 References 43

Figures

Figure 1. Behavior of trisodium phosphate dodecahydrate (TSPD)-saturated systems in graded electrolyte matrices at 20 and 30 °C. Columns compare carbonate-only (A, D, G, J, M), hydroxide-only (B, E, H, K, N), and mixed carbonate–hydroxide (C, F, I, L, O) systems. For each electrolyte regime, measured solution properties are shown as a function of final sodium concentration at equilibrium. Rows correspond to (top to bottom): dissolved phosphorus concentration as a function of final sodium, dissolved phosphorus concentration as a function of final pH, dynamic viscosity, density, and free hydroxide equivalents before and after equilibration with TSPD. Axes are shared within each row to facilitate comparison of suppression behavior across electrolyte regimes and temperatures. 13

Figure 2. Natrophosphate equilibration behavior at 20 °C with the starting solution at a constant total Na concentration of ~3.8 M. (A) Final dissolved phosphorus concentration. (B) Final dissolved phosphorus concentration as a function of pH. (C) Final dissolved fluoride concentration. (D) P/F ratio as a function of final dissolved sodium where the dashed line indicates stoichiometric dissolution (P/F = 2) and (E) P/F ratio as a function of pH. (F) Density before and after equilibration. (G) Dynamic viscosity before and after equilibration. (H) Free hydroxide before and after equilibration..... 18

Figure 3. Natrophosphate equilibration behavior at 20 °C with varying Na concentration. (A) Final dissolved phosphorus concentration. (B) Final dissolved phosphorus concentration as a function of pH. (C) Final dissolved fluoride concentration. (D) P/F ratio as a function of final dissolved sodium where the dashed line indicates stoichiometric dissolution (P/F = 2) and (E) P/F ratio as a function of pH. (F) Dynamic viscosity before and after equilibration. (G) Density before and after equilibration. (H) Free hydroxide before and after equilibration..... 21

Figure 4. Dissolved (A) aluminum, phosphorus, and fluoride and (B) sodium in a 3.8 M multicomponent sodium simulant as a function of time during progressive carbonate loading. (C) Free hydroxide equivalents, (D) density, (E) viscosity, (F) pH. 24

Figure 5. Dissolved (A) aluminum, (B) phosphorus, and (C) fluoride concentrations as a function of time for multicomponent simulant systems containing gibbsite alone and gibbsite in the presence of excess natrophosphate. (D) pH of the initial and final solutions after equilibration. Experiments were conducted with nano- and micro-scale gibbsite to evaluate particle-size effects on dissolution behavior. Phosphate and fluoride concentrations represent total dissolved concentrations including the initial solution composition..... 27

Figure 6. Dissolved (A) aluminum, (B) phosphorus, and (C) fluoride concentrations as a function of time following two-fold and four-fold dilution of clarified simulant solutions previously equilibrated with excess nanoparticle gibbsite, with and without excess natrophosphate. (D) pH of the solution immediately after dilution and the final time point (pt). Dilutions were performed after the systems approached steady behavior under the original high-ionic-strength matrix conditions..... 29

Figure 7. Concentration-dependent diffusivities of ^{31}P, ^{23}Na, and ^{1}H. 30

Figure 8. Potential of mean force diagram of Na_3PO_4 dimer. The x-axis is the distance between the two phosphorus atoms. 31

Figure 9. Water activity vs. the molality of aqueous sodium phosphate solutions at 298 K and 1 bar, for the M2019 and MT models. Red circles are experimental water activities (El Guendouzi and Benbiyi 2014). 32
Figure 10. Equilibration of an anhydrous Na_3PO_4 crystal with its 0.5 m solution. In this representation: green, pink, magenta, and yellow vdW spheres represent PO_4^{3-}, Na^+, HPO_4^{2-}, and OH^- ions, respectively. Water is represented with cyan points. 32
Figure 11. Concentration-dependent cluster size distribution of PO_4^{3-}–Na^+ contact ion pairs. 33
Figure 12. Residence time of PO_4^{3-} in solution clusters at different concentrations. 34
Figure 13. Snapshot from a simulation containing 216 Na^+, 59 PO_4^{3-}, 13 HPO_4^{2-}, 13 OH^-, and 20 NaF (using an unmodified M2019 force field for the description of fluoride). 35
Figure 14. $q4$ and $q6$ value distribution of the phosphates in anhydrous and dodecahydrate polymorphs of trisodium dodecahydrate. 36
Figure 15. Representation of disordered interfaces of liquid and (a) Na_3PO_4 anhydrous and (b) $Na_3PO_4 \cdot 12H_2O \cdot 1/6NaOH$ crystals with the MT force field. Green, pink, magenta, and yellow vdW spheres represent PO_4^{3-}, Na^+, HPO_4^{2-}, and OH^- ions, respectively. Water is represented with cyan points. 37
Figure 16. Predicted (line) aluminum concentration at 40 °C omitting enhancements arising from nanoparticle size and electrolytes beyond NaOH. The observed aluminum concentration (observed dot) is considerably below the expected Al concentration when solutions are saturated with gibbsite as the solubility-limiting phase. 38

Tables

Table 1. 3.8 M Na simulant composition (density = 1.14 g/cm^3). 4
Table 2. System dependent equilibration protocols. All systems are minimized prior to equilibration. 7
Table 3. Composition of concentration-dependent systems 7
Table 4. Composition of water activity systems 8
Table 5. System compositions for H_2O+Na_3PO_4+NaF. 11
Table 6. Estimated weight fractions of solid phases recovered from solubility experiments in solutions with varying Na concentration and TSPD in excess. Weight fractions are approximate because of strong preferred orientation. TSP = trisodium phosphate (Na_3PO_4). Empty cells are 0%. For Information Only. 15
Table 7. Estimated weight fractions of solid phases that were separated from solutions with fixed concentration of 3.8 M Na, with natrophosphate in excess. Two samples contained unidentified peaks; the remaining phases are scaled to 100%. Empty cells are 0%. For Information Only. 19
Table 8. Estimated weight fractions of solid phases separated from solutions with varying Na concentration, with natrophosphate in excess. Three samples contained unidentified peaks; the remaining phases are scaled to 100%. Empty cells are 0%. For Information Only. 22
Table 9. Estimated weight fractions of solid phases recovered from solubility experiments in simulant solutions with different added solids in excess. For Information Only 28
Table 10. Computed excess chemical potentials of water in aqueous sodium phosphate solutions. 31
Table 11. Concentration-dependent PO_4^{3-} - Na^+ first shell coordination numbers. 33
Table 12. D_P predicted in large clusters using a mixture model. 35
Table 13. Pre- and post-leach analytical results. 38
Table 14. Stage 1 and Stage 3 dilution analytical. 39

1.0 Introduction

Effective implementation of Direct Feed High-Level Waste (DFHLW) operations requires reliable control of solid–liquid equilibria in concentrated alkaline tank waste systems. In the southeast quadrant of the Hanford tank farms, large inventories of sparingly soluble phosphate- and fluoride-bearing solids, most notably natrophosphate [$Na_7F(PO_4)_2 \cdot 19H_2O$], coexist with gibbsite [$Al(OH)_3$] and trisodium phosphate (Na_3PO_4) (Colburn and Peterson 2021). The solid phases are in contact with high ionic-strength supernatants containing sodium salts of hydroxide (OH^-), phosphate (PO_4^{3-}), fluoride (F^-), nitrate (NO_3^-), nitrite (NO_2^-), carbonate (CO_3^{2-}), and aluminate ($Al(OH)_4^-$) (Miller and Britton 2017; Dembowski et al. 2020; Britton 2019b; Britton 2019a). The dissolution behavior of tank waste solids directly influences slurry density, rheology, solids transport, and overall system throughput.

Data in the literature has been examined to establish solubility trends as a function of Na concentration and temperature (Britton 2019a; Britton 2019b). However, current models based on these data cannot adequately predict the solubility of either phosphate or aluminum in multicomponent Hanford waste (Britton 2019a; Britton 2019b). The purpose of this work was to obtain solubility relationships between natrophosphate, gibbsite, and trisodium phosphate solid phases, and sodium carbonate-containing solutions at constant Na concentration. CO_3^2 is a major constituent of tank supernatants and can have a significant influence on PO_4^{3-} and $Al(OH)_4^-$ solubility (Reynolds et al. 2017). Because CO_3^{2-} participates in alkalinity buffering and modifies effective OH^- activity, it can alter dissolution equilibria in ways that are not captured by sodium concentration or ionic strength alone. The relative influence of CO_3^{2-} and OH^- on Na-PO_4^{3-} binding and PO_4^{3-} solubility in high-ionic-strength systems remains poorly resolved.

In this work, tests were designed to identify the influence of different electrolytes on solubility under progressively more complex chemical conditions. Natrophosphate solubility was measured in solutions containing mixtures of CO_3^{2-} and OH^- to establish the effect of electrolyte identity, both with a fixed total Na concentration (3.8 M) and with variable Na concentrations. Trisodium phosphate dodecahydrate solubility was then measured for comparison with natrophosphate to determine whether the trend in decreasing solubility as a function of electrolyte addition was the result of phosphate–alkalinity interactions or if fluoride from natrophosphate dissolution played a role. Tests were then extended to determine solubility of phosphate- and aluminum-bearing phases in multicomponent 3.8 M sodium simulants representative of high-PO_4^{3-} tank waste. Post-dissolution, the simulants were then perturbed via dilution. These tests evaluated equilibrium solubility behavior and phosphate stability under operationally relevant conditions. By isolating the contributions of carbonate concentration, hydroxide concentration, total sodium loading, and ionic strength, this work establishes experimentally constrained relationships between alkalinity partitioning and dissolution behavior.

The resulting dataset provides a foundation for refining empirical solubility models and informing molecular-scale simulations of ion association, activity effects, and competitive dissolution processes. More broadly, these results clarify how carbonate- and hydroxide-dominated alkalinity regimes influence phosphate stability in high-sodium waste streams. Together, these efforts advance predictive capability for solid–liquid equilibria under operationally relevant conditions and support development of processing strategies aimed at mitigating phosphate- and aluminum-driven transport limitations during DFHLW operations.

2.0 Quality Assurance

This work was performed in accordance with the Pacific Northwest National Laboratory (PNNL) Nuclear Quality Assurance Program (NQAP). The NQAP complies with the DOE Order 414.1D, *Quality Assurance*, and 10 CFR 830, Subpart A, *Quality Assurance Requirements*. The NQAP uses NQA-1-2012, *Quality Assurance Requirements for Nuclear Facility Applications*, as its consensus standard and NQA-1-2012, Subpart 4.2.1, as the basis for its graded approach to quality.

The NQAP works in conjunction with PNNL's laboratory-level Quality Management Program, which is based on the requirements as defined in the DOE Order 414.1D and 10 CFR 830, Subpart A. This work was conducted at technology readiness level 3, corresponding to experimental proof-of-concept under controlled laboratory conditions. As such, the results are intended to establish fundamental solubility relationships and mechanistic understanding and are not directly representative of full-scale process conditions.

3.0 Materials and Methods

3.1 Reagents

Aqueous media for all solubility experiments were prepared with nitrogen-sparged deionized (DI) water (18.2 MΩ·cm). Trisodium phosphate dodecahydrate (TSPD) was recrystallized prior to experimental use to ensure a consistent hydration state of the solid phase as demonstrated with XRD (ITSW-DP-017). . All other reagents were used as supplied without further purification. Chemicals included sodium nitrate ($NaNO_3$, ≥99%), sodium fluoride (NaF, ≥99%), sodium phosphate dodecahydrate ($Na_3PO_4 \cdot 12H_2O$, ≥98%), sodium chloride (NaCl, 99%), potassium chloride (KCl, ≥99%), sodium hydroxide (50% w/w NaOH), sodium nitrite ($NaNO_2$, 99%), sodium carbonate (Na_2CO_3, 99%), sodium aluminate ($NaAlO_2$, ≥99%), and aluminum nitrate nonahydrate [$Al(NO_3)_3 \cdot 9H_2O$, ≥98%], all obtained from Sigma-Aldrich.

3.2 Gibbsite Synthesis

Nanoscale gibbsite was synthesized using neutralization of an acidic aluminum solution followed by hydrothermal treatment as reported previously (Zhang et al. 2017). An aqueous 0.25 M $Al(NO_3)_3 \cdot 9H_2O$ solution was titrated to approximately pH 5 with 1 M NaOH, producing a gelatinous aluminum hydroxide precipitate. The suspension was stirred for 1 h at ambient temperature and the solid phase was isolated by centrifugation. The precipitate was subsequently redispersed in DI water, washed, and recentrifuged through three sequential purification cycles. The washed material was transferred to a Teflon-lined Parr reactor containing DI water and subjected to hydrothermal treatment at 80 °C with slow rotation (~10 rpm). After 72 h, the resulting gibbsite nanoplates were recovered by centrifugation, rinsed three times with DI water, and dried overnight at 60 °C.

3.3 Natrophosphate Synthesis

Natrophosphate crystals were prepared by cooling a mixture of concentrated solutions (Graham et al. 2022). NaF (84 g) was dissolved in 1 L of DI water to generate the fluoride stock solution. In a separate vessel, 164 g of TSPD was dissolved in 20 g of DI water to prepare a concentrated phosphate solution. Both solutions were heated to near their boiling temperatures and combined under vigorous stirring. After 60 min of mixing, agitation was stopped and the solution was allowed to cool gradually to approximately 20 °C over a 20-h period. The cooled mixture was subsequently aged at 5 °C for 24 h to promote crystallization. The precipitated natrophosphate solids were isolated by vacuum filtration. The materials were not dried before use in order to preserve the crystallographic hydration of natrophosphate.

3.4 Simulant Preparation

Simulant solutions were prepared in 100-mL volumetric flasks at controlled temperatures of 20 or 36 °C. Reagents were introduced sequentially in order of increasing solubility to facilitate complete dissolution (Table 1). Each preparation began with 30 mL of DI water, followed by addition of 50% w/w sodium hydroxide stock solution, sodium fluoride, potassium chloride, sodium nitrite, sodium nitrate, sodium phosphate dodecahydrate, and sodium carbonate. DI water was then added to bring the mixture to final volume. After each addition, the solution was allowed to equilibrate until the solid phase was fully dissolved. For the final components in the sequence, a minimum dissolution period of 30 min was enforced prior to introducing the next reagent. Upon completion of reagent addition, the solutions were stirred overnight to ensure homogeneity. Some preparations exhibited undissolved residual solids that were difficult to remove using standard techniques.

Clarification methods evaluated included 0.2-µm nylon syringe filtration, centrifugation, and vacuum filtration. Final simulants were filtered using 0.45-µm polypropylene syringe filters at a ratio of one filter per 10 mL of solution and were equilibrated at the target temperature (20 or 36 °C) prior to use. Bulk compositions of all prepared solutions were verified by inductively coupled plasma-optical emission spectrometry (ICP-OES) and ion chromatography (IC) before initiating solubility experiments.

Table 1. 3.8 M Na simulant composition (density = 1.14 g/cm^3).

Component	Molecular Weight (g/mol)	Anion/Cation Species	Target Conc. (M)
NaF	41.99	F^-	0.07
Na_3PO_4-12H_2O	380.10	PO_4^{3-}	0.09
$NaNO_2$	69.00	NO_2^-	1.06
$NaNO_3$	84.99	NO_3^-	0.71
NaOH (50% solution, w/w)	40.00	Free OH^-	0.29
Na_2CO_3	106.0	CO_3^{2-}	0.65
$NaAlO_2$	81.97	Al^{3+}	0.009
KCl	74.55	K^+	0.03

3.5 Apparatus for Solubility Experiments

Stock electrolyte solutions were prepared by dissolving the appropriate sodium salts in DI water and equilibrating them at either 20 or 30 °C prior to solid addition. Solubility tests were initiated under saturated conditions by introducing excess gibbsite based on reported solubility constraints (Misra 1970). For natrophosphate systems, incremental additions were required to ensure that solid loading exceeded the anticipated solubility limit. Experiments were performed in triplicate within an N_2-filled glovebox to limit atmospheric CO_2 uptake in the alkaline matrices. Reaction mixtures were contained in Teflon vessels positioned within an aluminum bead bath housed on a temperature-controlled stir plate. Continuous mixing was maintained at 250 rpm using polytetrafluoroethylene-coated magnetic stir bars. Thermal stability during equilibration was controlled within ±2 °C and verified with National Institute of Standards and Technology–traceable calibrated thermometers.

3.6 Sampling Solubility Experiments

Aliquots were withdrawn at equilibration temperature using pipette tips preconditioned to match the solution temperature. Approximately 1.0 mL of solution was collected from each reaction vessel and immediately passed through preheated 0.2-µm nylon filters to minimize temperature-induced perturbations during separation. Samples were collected at approximately 24-h intervals until equilibrium was achieved, operationally defined as three consecutive concentration measurements exhibiting no systematic variation. Reported solubility values correspond to the mean of triplicate analytical determinations for each of three independent experimental replicates (n = 9 total) conducted at nominal temperatures of 20 and 30 °C. Actual sampling temperatures were verified through calibration against the established solubility of KNO_3, yielding effective temperatures of 20 and 30 °C (Zhu et al. 2020). All temperatures referenced herein reflect these calibrated values.

Immediately following filtration, samples were serially diluted with DI water prior to instrumental analysis. An initial six-fold dilution was performed, followed by a subsequent 21-fold dilution, yielding a cumulative dilution factor of 168× for routine ICP-OES and IC measurements. For selected

samples requiring extended analytical range for IC determination of Cl^-, PO_4^{3-}, NO_2^-, and NO_3^-, additional dilution steps were applied. Final dilution factors for these cases were adjusted to 840×, 1,680×, or 16,800× as required to bring analyte concentrations within the calibration window.

Upon attaining equilibrium, systems containing excess natrophosphate were carefully decanted and the supernatant was passed through 0.2-µm nylon syringe filters to remove residual undissolved solids. The retained natrophosphate solids were transferred to sterile cell filters, allowed to drain under gravity, and collected for subsequent characterization. For experiments containing excess gibbsite, solid–liquid separation was performed using a Cole-Parmer polypropylene filtration assembly fitted with a 25-mm, 0.2-µm nylon membrane. At elevated NaOH concentrations, where filtration efficiency was reduced, centrifugation was employed to facilitate phase separation. Recovered solids were removed from the filter medium, transferred to weigh boats, and dried prior to storage and future analysis. Clarified supernatant solutions were subdivided into separate aliquots for measurement of total alkalinity, total carbon, pH, density, and viscosity.

3.7 Solution Phase Analysis

All chemical analyses were conducted at the Analytical Analysis Center in the PNNL Bioproducts, Sciences, and Engineering Laboratory. Aluminum and phosphorus concentrations were quantified by ICP-OES using a PerkinElmer Avio 550 instrument configured with a Meinhard nebulizer, glass cyclonic spray chamber, and 2.0-mm alumina injector. Data acquisition and processing were performed with Syngistix software (version 5.5). Calibration curves were generated from certified reference standards and independently verified with secondary standards. Calibration and quality control checks were performed daily. Samples were diluted with DI water or dilute nitric acid (for Al analysis) as required to maintain analyte concentrations within the validated calibration range. All standards and samples were analyzed in triplicate. Matrix spike standards of known mass composition were included to confirm analytical recovery. Method performance and associated uncertainties were evaluated and documented as part of the analytical quality assurance process. Nitrite, nitrate, fluoride, and chloride concentrations were determined using a Dionex Reagent-Free Ion Chromatography System 5000 (RFICS-5000) equipped with an autosampler (model AS-AP). Measurements of pH, density, and dynamic viscosity were conducted at variable temperature using a Fisher Accumet XL150 pH meter, a Mettler Toledo Easy D40 densimeter, and an Anton Paar Lovis 2000 M micro viscometer.

3.8 Variable Temperature Raman Spectroscopy

Raman spectra of sodium phosphate solutions were recorded over a 5-s integration time using a MarqMetrix spectrometer (Thermo Scientific) with an immersion probe and a 785-nm laser operated at 300 mW. The solutions were heated in a glass vessel with a tight-fitting cap held in an aluminum bead bath on a laboratory hot-plate stirrer running at 300 rpm. The Raman and a temperature probe were inserted through the cap using silicone grommets. Peak areas were determined by fitting pseudo-Voight profiles to the observed resonances with a fifth-order Chebyshev background between Raman shift frequencies of 800 and 1200 cm^{-1}.

3.9 Variable Temperature PFG-NMR Spectroscopy

Pulsed-field gradient (PFG) stimulated echo nuclear magnetic resonance (NMR) spectra were acquired using the DgcsteSL_cc pulse sequence on an 11.7434 T Agilent/Varian NMR spectrometer equipped with a broadband probe. Temperature calibration was performed using the ^1H chemical shifts of a flame-sealed ethylene glycol standard. Samples were allowed to equilibrate for

approximately 30 min following each temperature adjustment prior to data acquisition. For all nuclei, diffusion experiments were conducted using a diffusion delay (Δ) of 50 ms. The diffusion encoding gradient pulse duration (δ) was optimized at each temperature. Diffusion coefficients were calculated from integrated signal intensities using a single-component model.

For ^{1}H, the acquisition time was 5 s, and eight transients were collected at each gradient increment. Sixteen steady-state pulses were applied, and the recycle delay between scans was 10 s. A total of 18 gradient increments were used. The π/2 pulse length was 12.25 μs, and δ was approximately 1 ms. The total experimental time was approximately 40 min per sample. No truncation of the free induction decay (FID) was applied and then 5 Hz of exponential line broadening was applied.

For ^{23}Na, the acquisition time was 1 s, and 128 transients were collected at each gradient increment. Four steady-state pulses were applied, and the recycle delay between scans was 1 s. A total of 16 gradient increments were used. The π/2 pulse length was 12.3125 μs, and δ was approximately 4.8 ms. The total experimental time was approximately 70 min per sample. No truncation of the FID was applied and then 5 Hz of exponential line broadening was applied.

For ^{31}P, the acquisition time was 5 s, and 32 transients were collected at each gradient increment. Sixteen steady-state pulses were applied, and the recycle delay between scans was 5 s. A total of 18 gradient increments were used. The π/2 pulse length was 16.5 μs, and δ was approximately 5 ms. The total experimental time was approximately 99 min per sample. The FID was truncated to 128,000 points prior to processing and then 5 Hz of exponential line broadening was applied.

3.10 X-ray Diffraction

Powder X-ray diffraction patterns were collected using a Rigaku SmartLab SE θ–2θ diffractometer equipped with a Cu sealed anode X-ray source (λ = 1.5418 Å) operating at 40 kV and 44 mA and a one-dimensional semiconductor detector. Data were recorded with a step size of 0.01° at a scan rate of 1.8° min^{-1} using zero-background sample holders housed in atmosphere-protected cells supplied by Rigaku. Rietveld refinement of the diffraction data was performed using TOPAS v6 (Bruker AXS).

3.11 Simulations

3.11.1 Simulation Details

Classical molecular dynamics simulations of phosphate systems were conducted using the classical force fields that were developed in the first year of this project. The two models, referred to as M2019 (Madrid2019) and MT (Madrid Transport), use TIP4P/2005 water model (Abascal and Vega 2005). AMBER PO_4^{3-} and HPO_4^{2-} anions are combined with M2019 and MT Na^+ and OH^- models, respectively (Zeron et al. 2019; de Lucas et al. 2024; Steinbrecher et al. 2012; Blazquez et al. 2023; Habibi et al. 2022). Simulations were performed using the 2024.2 package of GROMACS MD software (Abraham et al. 2024).

All simulations were minimized and equilibrated prior to data collection with system-based equilibration protocols given in Table 2. All temperature coupling was done using the velocity rescale thermostat (Bussi et al. 2007) and all pressure coupling was done using the cell resizing barostat (Bernetti and Bussi 2020) unless indicated otherwise. The timestep for the simulations was 1 fs with neighbor lists updated every 20 fs. The van der Waals (vdW) interactions were truncated at 10Å, whereas coulombic interactions were treated with the Particle Mesh Ewald method of order 4 beyond 10 Å with a Fourier grid spacing of 1.6 Å. All simulations are performed at 293 K and 1 bar. Sampling was done with a dump frequency of 1 ps.

Table 2. System dependent equilibration protocols. All systems are minimized prior to equilibration.

System	System Size in nm	Equilibrium Protocol
Concentration-dependent simulations	(7.1 7.1 7.1)	5 ns NVT at 310 K + 10ns NPT 310K→ 293K + 5 ns NPT + 5 ns NVT + 10 ns NPT + 10 ns NVT
Solid simulations	Na_3PO_4 : (20.2, 2.0, 3.2) $Na_3PO_4 \cdot 12H_2O \cdot 1/6NaOH$: (20.8, 3.0, 2.5)	Heated in NPT ensemble from 1K → 293K linearly in 300 ns + 100 ns
Solubility	Twice the solid size (solid+liquid)	Relaxed for 1 ps with Berendsen barostat (Berendsen et al. 1984)
Potential energy surface simulations	(4.5, 4.5, 4.5)	15 ns NVT + 15 ns NPT + 15 ns NVT at 293K
Water activity simulations	(3.1, 3.1, 3.1)	8 ns NVT + 8 ns NPT at 293K

All liquid initial structures were created using PACKMOL (Martínez et al. 2009). The compositions of simulated systems were calculated based on the number of water molecules set for the simulations. The number of PO_4^{3-}, HPO_4^{2-}, and OH^- simulated systems was calculated using the pH measurements at the given concentration with the equation pOH = -log[OH].

Concentration-dependent systems are set up accounting for speciation of phosphate anions into hydrogen phosphate and hydroxide anions. The simulated system compositions are given in Table 3.

Table 3. Composition of concentration-dependent systems

Molality (m)	# of H_2O	# of Na^+	# of PO_4^{3-}	# of HPO_4^{2-}	# of OH^-
0.1	11997	66	19	3	3
0.2	11996	129	39	4	4
0.3	11996	195	61	4	4
0.4	11996	261	83	4	4
0.5	11996	324	104	4	4
0.6	11996	390	126	4	4
0.7	11996	453	147	4	4

3.11.2 Radial Distribution Functions

Radial distribution functions of each pair are calculated using the *gmx rdf* tool with the relation

$$g_{AB}(r) = \frac{\langle \rho_B(r) \rangle}{\langle \rho_B \rangle_{local}} = \frac{1}{\langle \rho_B \rangle_{local}} \frac{1}{N_A} \sum_{i \in A}^{N_A} \sum_{j \in B}^{N_B} \frac{\delta(r_{ij} - r)}{4\pi r^2} \quad (1)$$

where $\langle \rho_B(r) \rangle$ is the density of particle type B at a distance r around particles A, $\langle \rho_B \rangle_{local}$ is the averaged type B particle density over all spheres around particle A with radius r_{max}, N_A and N_B are the number of A and B particles in the system, respectively. Finally, r_{ij} is the instantaneous distance between particles *i* and *j*, whereas r is the specified bin distance. The δ term measured the deviation in distance from *r*. Integrating the area under $g_{AB}(r)$ yields the coordination number of the pair at distance r.

3.11.3 Diffusion Coefficients

The diffusion coefficients D_A of particles of type A, are calculated using the Einstein relation:

$$\lim_{t\to\infty}\langle\|r_i(t)-r_i(0)\|^2\rangle_{i\in A}=6D_At \quad (2)$$

The fit to the mean square displacement slope is started at 10% of the trajectory until 90% of the trajectory using gmx msd tool. In this equation, t is simulation time, $r_i(t)$ and $r_i(0)$ are the position of particle at time t and time 0, respectively, and D_A is the diffusion of particle A.

3.11.4 Umbrella Sampling Simulations

A simulation box of 3000 waters and two Na_3PO_4 ions without speciation was created. For both models, systems were equilibrated without any restraints, as given in Table 2. The distance between center atoms of phosphates was chosen as the collective variable to sample through. Eleven windows of 1 Å bin width were created between 5-12 Å. After the initial equilibration, the phosphates were gently pulled to the designated distance with a small biasing force constant value of 80 kcal/mol. Then, the biasing force constant was set to 145 kcal/mol and each window was simulated for 5 ns. Weighted Average Histogram Algorithm Method software (WHAM, version 2.0.10.1) was used to obtain the relative energetics of each sampled configurational space window.

3.11.5 Water Activities

The concentrations of the water activities of aqueous sodium phosphate solutions were calculated and are given in Table 4.

Table 4. Composition of water activity systems

Molality ($\boldsymbol{m}$)	# of H_2O	# of Na^+	# of PO_4^{3-}	# of HPO_4^{2-}	# of OH^-
0.3	1000	15	4	1	1
0.5	1000	27	7	2	2
0.6	1000	33	9	2	2

The water activities (a_w) have been computed using (Hempel et al. 2012; Habibi et al. 2024):

$$a_w=\frac{\langle\rho_{w,m}\rangle}{\langle\rho_{w,m=0}\rangle}exp\left[\frac{\left(\mu_{w,m}^{ex}-\mu_{w,m=0}^{ex}\right)}{k_BT}\right] \quad (3)$$

where $\langle\rho_{w,m}\rangle$ and $\langle\rho_{w,m=0}\rangle$ are the ensemble average of number densities of water at molalities m and 0, respectively, and k_B is the Boltzmann constant. Here $\mu_{w,m}^{ex}$ and $\mu_{w,m=0}^{ex}$ are the excess chemical potentials of water at molalities m and 0, respectively, and T is the temperature in Kelvin.

The excess chemical potentials have been obtained from the negative free energy changes resulting from gradually turning off the interactions of a water molecule from the solution. Lennard-Jones (LJ) and coulombic interactions are expressed as functions of a coupling parameter (λ for LJ and ϕ for coulombic interactions). To prevent large fluctuations in the potential and the computational instabilities, we turned off the Coulombic interactions first with 20 windows, $\phi=[0, 0.05, 0.10, \ldots, 0.90, 0.95, 1]$. Followed by gradually turning off the LJ interactions with 20

windows, $\lambda = [0, 0.05, 0.10, \ldots, 0.90, 0.95, 1]$. The Bennett acceptance ratio (BAR) method (Bennett 1976) was then employed to obtain free energy changes. At each window, the activation energies were sampled from a 50-ns production run in NPT (isothermal–isobaric ensemble (constant number of particles, pressure, and temperature) ensemble.

3.11.6 Solid Simulations

The models used in this work are parametrized at 70% scaled charges, where the total charge on any ion is reduced to 70% of its formal value. This technique, known as electronic continuum correction, is implemented to improve the solution behavior of electrolyte solutions by mimicking the water screening effects that are missing in classical molecular dynamics simulations. Phosphate ions highly benefit from this approach; the scaling of charges significantly decreases the highly overestimated aggregating of these. However, this method weakens the relative forces between ions and may not improve the solid phase properties.

Anhydrous Na_3PO_4 crystal unit cell is made into a supercell with visual molecular dynamics (Humphrey et al. 1996). The missing hydrogens of $Na_3PO_4 \cdot 12H_2O \cdot 1/6NaOH$ unit cell were added using Pymol (The PyMOL Molecular Graphics System, Version 3.0 Schrödinger, LLC.) The added hydrogens were relaxed using PBE/DZVP-MOLOPT-SR-GTH level of theory. The broken bonds due to periodicity were healed and the file format was edited, and a supercell was created using visual molecular dynamics.

To understand the ability of force fields in creating stable solid phases, Steinhardt parameters were used (Steinhardt et al. 1983). Also known as bond orders, these parameters were used to differentiate solid phases and to identify liquid and solid phases. They evaluate the local symmetry of the central atoms, phosphate for this case, using spherical harmonics, yielding a value between 0 and 1. The Steinhardt parameter, q_l, is calculated as

$$q_l(i) = \sqrt{\frac{4\pi}{(2l\ +\ 1)} \sum_{m=-l}^{l} |q_{lm}(i)|^2} \tag{4}$$

and

$$q_{lm}(i) = \frac{1}{N(i)} \sum_{j=1}^{N(i)} Y_{lm}(r_{ij}) \tag{5}$$

where N(i) is the number of nearest neighbors for particle i, r_{ij} is the vector connecting particle i to neighbor j, and Y_{lm} is the spherical harmonic function with degree l and order m ($m \in [-l,+l]$).

In real systems, the effect of thermal vibrations causes atomic positions to fluctuate. Calculating the q_l of such a system may yield a very noisy distribution in which identifying the crystal phases is difficult. To address this, Lechner and Dellago (2008) proposed the averaged Steinhardt parameters, $\bar{q}_l$. These averaged bond orders are calculated as

$$\bar{q}_l(i)\ =\ \sqrt{\frac{4\pi}{(2l\ +\ 1)} \sum_{m=-l}^{l} \left| \frac{1}{\tilde{N}(i)} \sum_{k=1}^{\tilde{N}(i)} q_{lm}(k) \right|^2} \tag{6}$$

where k is an index over the $\widetilde{N}(i)$ particles in the local environment of particle i, including particle i itself and all of its neighboring particles. Here, $\widetilde{N}(i)$ represents the total number of particles in this local environment. The averaged bond order parameter $\bar{q}_l(i)$ therefore incorporates contributions from both the first coordination shell and the surrounding local structure. This averaging reduces overlap between bond order distributions and improves discrimination between different crystal structures. In this work, these averaged bond order parameters were used to differentiate between crystalline phases.

3.11.7 Solid-Liquid Interfacial Systems

For measuring the solubility of models, the direct coexistence method was used. In this method, the equilibrated crystal is put in contact with its equilibrated near-saturation solution and simulated until equilibrium is reached. The results obtained from the direct coexistence method are known to be significantly impacted by the system size. Two important sizes considerations here are (1) having a solid that is thick enough to not be destabilized and thus dissolve fully by the liquid, and (2) having a large enough contact surface area of the liquid and solid phases. Failing to meet these requirements will result in either a fully destabilized solid structure that is no longer the crystal structure of interest or an artificially high solubility measurement.

The system sizes were benchmarked considering these two necessities prior to choosing the reported system sizes reported in Table 2. For all interfacial simulations, an anisotropic Parrinello-Rahman barostat was used (Parrinello and Rahman 1981).

The equilibrium was defined as where the number of ions in solutions starts fluctuating around the same number. The number of particles in solution ($m_{Na_3PO_4,approx}$) was tracked by the equation

$$m_{Na_3PO_4,approx} = \frac{N_{total,ions} - N_{solid,ions}}{4M_wN_w} \quad (7)$$

where the number of ions in solution was estimated by the difference in the number of total ions ($N_{total,ions}$) and the number of ions identified as solid $N_{solid,ions}$). In this equation, the division by 4 accounts for a single Na_3PO_4 unit, M_w is 0.018 015 kg/mol, and N_w is the number of liquid waters in the system. The distinction of solid vs. liquid ions was done by using a cutoff in the Steinhardt parameter distribution. Once the simulations reach equilibrium the mass density profiles were calculated using the *gmx density* tool of GROMACS. The equation

$$m_{Na_3PO_4} = \frac{\rho_z^{ions}}{\rho_z^{water}M_s} \quad (8)$$

was used to determine the final solubility value of each crystal in each force field. Here, M_s is the weight of 1 Na_3PO_4 molecule= 0.16394 kg/mol, ρ_z^{water} and ρ_z^{ions} are the mass density of water and ions, respectively. This methodology of measuring solubility was adapted from the work of Espinosa et al. (2016)

3.11.8 Phosphate Systems with Fluoride

Initial force field compatibility tests were performed with a charge down-scaled M2019 F^- model to match the rest of the force field charges. Preliminary systems were set without considering the effect of NaF on the speciation of Na_3PO_4. The system compositions are given in Table 5.

Table 5. System compositions for H_2O+Na_3PO_4+NaF.

Na_3PO_4 Concentration ($\boldsymbol{m}$)	# of H_2O	# of Na^+	# of PO_4^{3-}	# of HPO_4^{2-} = # of OH^-	# of F^-
0.2	8000	96	23	3	10
0.2	8000	96	23	3	20
0.5	8000	216	59	4	10
0.5	8000	216	59	4	20

4.0 Solubility Results

This section presents the results from solubility tests with TSPD, natrophosphate, and gibbsite. Solution-phase concentrations of phosphorus, fluoride, aluminum, and sodium are reported to define dissolution behavior and identify influences on solubility. Phosphorus concentrations were measured as total dissolved phosphorus. However, under the highly alkaline conditions of this study, dissolved phosphorus is expected to be present predominantly as PO_4^{3-} and is therefore discussed as phosphate where appropriate. Supporting physicochemical measurements and solid phase characterization are included to confirm system stability and composition.

4.1 Trisodium Phosphate Dodecahydrate Solubility in Solutions with Varying Sodium Concentration

4.1.1 Solution Phase Data

TSPD dissolution was examined to determine whether the carbonate- and hydroxide-dependent effects on phosphate solubility observed with natrophosphate are a general feature of phosphate–alkalinity interactions or instead arise in part from concurrent fluoride dissolution. As shown in Figure 1, addition of electrolytes decreased TSPD dissolution, resulting in lower dissolved phosphorus concentrations. In carbonate-containing solutions, dissolved phosphorus decreased gradually as Na_2CO_3 concentration increased from 0.4 to 1.2 M at 30 and 20 °C, while measured final sodium concentrations increased proportionally, producing an approximately linear relationship between dissolved phosphorus and final sodium concentration.

TSPD solubility was uniformly higher at 30 °C than at 20 °C, but the suppression trend with increasing carbonate loading was preserved. In hydroxide-only matrices, increasing NaOH concentration produced a sharp decrease in dissolved phosphorus while measured final sodium concentrations remained near approximately 1 M. When plotted as a function of final sodium concentration, this behavior appears as a near-vertical decrease in dissolved phosphorus, indicating that additional NaOH suppresses phosphate dissolution without producing proportional increases in dissolved sodium.

Mixed carbonate–hydroxide systems exhibited intermediate suppression behavior between the carbonate-only and hydroxide-only regimes. At 20 °C, dissolved phosphorus concentrations in the mixed systems were lower than those observed in either single-electrolyte system at comparable nominal concentrations, although total base loading was correspondingly higher. At 30 °C, dissolved phosphorus remained nearly constant between 0.8 and 1.2 M mixed base despite a modest increase in measured sodium concentration. Across both temperatures, the ordering of suppression behavior remained consistent, with hydroxide-dominated systems producing the strongest decrease in dissolved phosphorus, mixed systems with intermediate behavior, and carbonate-only systems the weakest suppression.

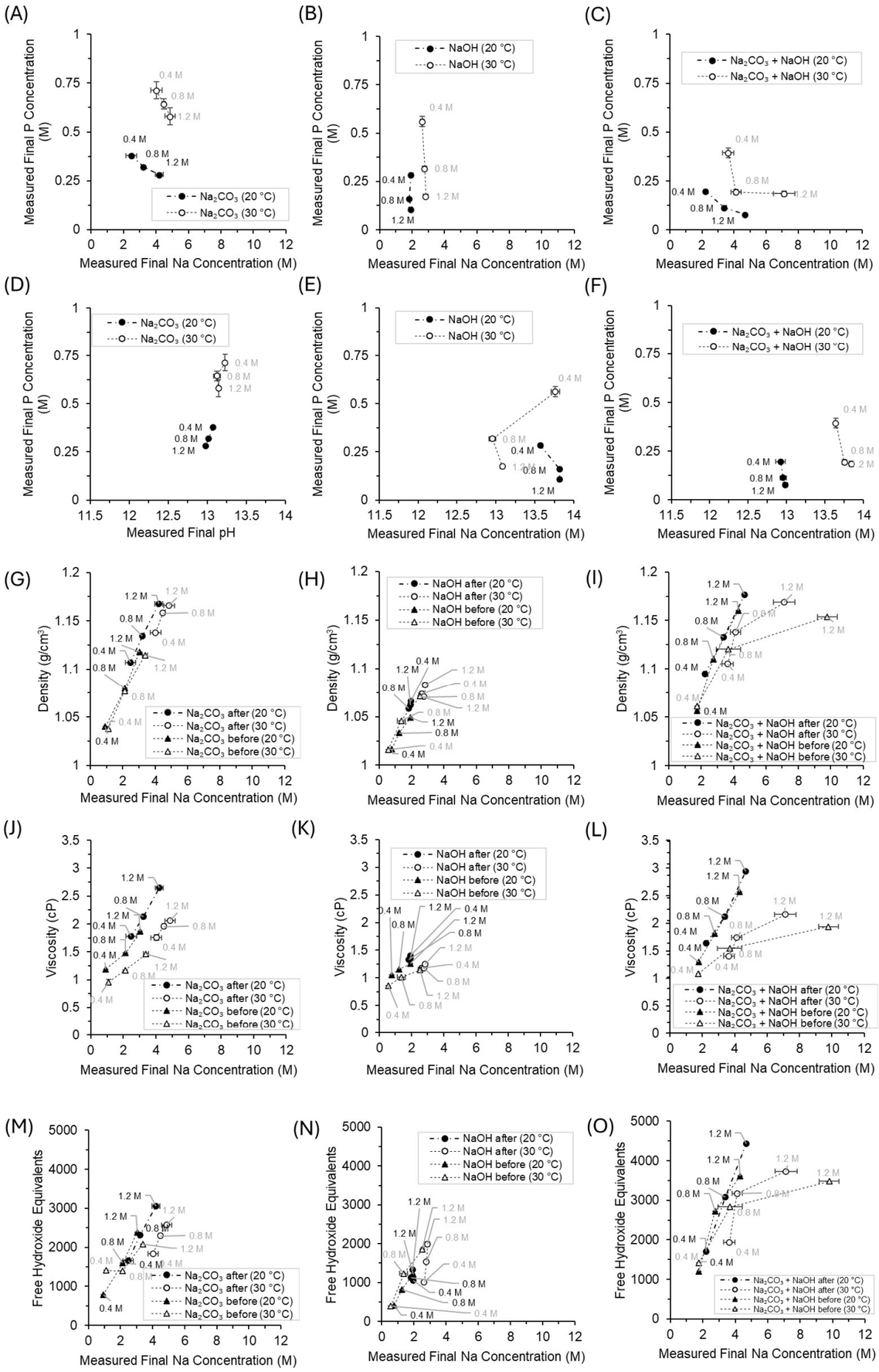

Figure 1. Behavior of trisodium phosphate dodecahydrate (TSPD)-saturated systems in graded electrolyte matrices at 20 and 30 °C. Columns compare carbonate-only (A, D, G, J, M), hydroxide-only (B, E, H, K, N), and mixed carbonate–hydroxide (C, F, I, L, O) systems. For each electrolyte regime, measured solution properties are shown as a function of final sodium concentration at equilibrium. Rows correspond to (top to bottom): dissolved phosphorus concentration as a function of final sodium, dissolved phosphorus concentration as a function of final pH, dynamic viscosity, density, and free hydroxide equivalents before and after equilibration with TSPD. Axes are shared within each row to facilitate comparison of suppression behavior across electrolyte regimes and temperatures.

Across graded electrolyte compositions, the contrasting sodium–phosphate relationships indicate that hydroxide- and carbonate-dominated systems occupy different dissolution regimes. In hydroxide-only matrices, increasing NaOH suppresses phosphate dissolution while dissolved sodium concentrations remain near 1 M, indicating that the system enters a phosphate-limited regime in which additional base does not produce proportional increases in dissolved sodium. In contrast, carbonate-only systems allow dissolved sodium to increase with carbonate loading while dissolved phosphorus concentrations decrease more gradually, indicating a weaker solubility penalty under increasing alkalinity. These results show that hydroxide-rich systems strongly constrain phosphate dissolution, whereas carbonate-containing matrices permit continued sodium accumulation in solution. The hydroxide-driven suppression behavior observed for TSPD is consistent with trends identified for natrophosphate under fixed 3.8 M sodium conditions, where increasing hydroxide loading likewise did not elevate dissolved phosphorus concentrations and solution composition exhibited limited sensitivity to additional NaOH.

4.1.2 Solid Phase Characterization

Solids recovered from TSPD systems were analyzed by X-ray powder diffraction to evaluate phase identity across graded carbonate-only, hydroxide-only, and mixed electrolyte matrices. Semi-quantitative weight fractions of the solid phases are given in Table 6. These values are approximate because strong preferred orientation and the handling sensitivity of hydrated phases precluded rigorous quantitative analysis with an internal standard. At 20 °C, TSPD was the dominant phosphorus-bearing crystalline phase in all systems examined. No alternative phosphate polymorphs or secondary phosphate-containing solids were detected. In selected samples, reflections consistent with trisodium phosphate heptahydrate ($Na_3PO_4 \cdot 7H_2O$) were observed.

Prior work has demonstrated that TSPD undergoes partial dehydration to the heptahydrate upon exposure to atmospheric conditions during handling and drying. Because solids were recovered and processed under ambient conditions, the presence of the heptahydrate is attributed to post-collection dehydration rather than to equilibrium stabilization of a lower hydrate form under the experimental solution conditions. Hydrates containing less water were prevalent in the 30 °C samples, and this is attributed to dehydration during post-separation handling and drying at elevated temperature, consistent with prior observations of trisodium phosphate hydrate transformations under ambient conditions (Graham et al. 2026). On this basis, TSPD is inferred to be the controlling solid phase at both 20 and 30 °C in the examined electrolyte matrices.

Variations in relative diffraction peak intensities were observed among samples. The recovered trisodium phosphate crystals exhibited columnar morphology which promotes preferred orientation during sample mounting and is therefore expected. Phase identification was based on peak positions and pattern matching rather than on relative intensity ratios, and no evidence of structurally distinct phosphate polymorphs or carbonate-substituted phosphate phases was identified. Accordingly, reported phase fractions are semi-quantitative estimates and should be interpreted as approximate due to preferred orientation effects.

The electrolyte-dependent suppression trends observed in solution were interpreted as a consequence of solution-phase thermodynamic effects rather than transformation of the phosphate solid phase, as no systematic changes in the identity of the phosphate-bearing crystalline phases were observed across the electrolyte conditions examined. Sodium carbonate was also observed as the monohydrate in some of the samples. It was more prevalent for samples equilibrated at 30 °C and those with higher initial quantities of carbonate.

Table 6. Estimated weight fractions of solid phases recovered from solubility experiments in solutions with varying Na concentration and TSPD in excess. Weight fractions are approximate because of strong preferred orientation. TSP = trisodium phosphate (Na_3PO_4). Empty cells are 0%. For Information Only.

$Na_3(PO_4)\cdot 12H_2O$ in excess, 20 °C							
Solution	Na (mol L^{-1})	TSPD	TSP·$7H_2O$	TSP·$6H_2O$	TSP·$0.5H_2O$	$Na_2CO_3\cdot H_2O$	$NaNO_3$
0.4 M Na_2CO_3	0.8	100%					
0.8 M Na_2CO_3	1.6	100%					
1.2 M Na_2CO_3	2.4	100%					
0.4 M NaOH	0.4	100%					
0.8 M NaOH	0.8	100%					
1.2 M NaOH	1.2	50%	50%				
0.4 M Na_2CO_3 + 0.4 M NaOH	1.2	100%					
0.8 M Na_2CO_3 + 0.8 M NaOH	2.4	100%					
1.2 M Na_2CO_3 + 1.2 M NaOH	3.6	85%				15%	
3.8 M $NaNO_3$	3.8		80%				20%
$Na_3(PO_4)\cdot 12H_2O$ in excess, 30 °C							
Solution	Na (mol L^{-1})	TSPD	TSP·$7H_2O$	TSP·$6H_2O$	TSP·$0.5H_2O$	$Na_2CO_3\cdot H_2O$	$NaNO_3$
0.4 M Na_2CO_3	0.8				89%	11%	
0.8 M Na_2CO_3	1.6				82%	18%	
1.2 M Na_2CO_3	2.4				80%	20%	
0.4 M NaOH	0.4				100%		
0.8 M NaOH	0.8			24%	76%		
1.2 M NaOH	1.2				100%		
0.4 M Na_2CO_3 + 0.4 M NaOH	1.2			100%			
0.8 M Na_2CO_3 + 0.8 M NaOH	2.4			80%	20%		
1.2 M Na_2CO_3 + 1.2 M NaOH	3.6			80%		20%	
3.8 M $NaNO_3$	3.8	80%					20%

4.1.3 Physicochemical Characterization

Bulk density, dynamic viscosity, and free hydroxide equivalents were measured before and after equilibration to document changes in solution properties accompanying saturation and to confirm that electrolyte-dependent suppression trends were not artifacts of bulk solution behavior. Across carbonate-, hydroxide-, and mixed-electrolyte systems, solution density exhibited an approximately linear relationship with measured final sodium concentration (Figure 1). Equilibration with trisodium phosphate dodecahydrate produced modest density increases relative to the initially prepared solutions, but both pre- and post-equilibration values followed nearly the same density–sodium trendline. Densities of carbonate-containing systems were consistently higher than those of hydroxide-only systems across the examined concentration range, reflecting the greater sodium content associated with carbonate salts. Densities measured at 30 °C were similar to those at 20 °C despite higher dissolved solids at saturation, indicating that the opposing effects of increased salt loading and thermal expansion largely offset one another.

Dynamic viscosities increased systematically with measured final sodium concentration across all electrolyte regimes. The dependence was approximately linear over the experimental range, although the relationship was slightly steeper at higher sodium concentrations. At each nominal base concentration, viscosities after equilibration with trisodium phosphate dodecahydrate were higher than those of the initially prepared solutions, consistent with increased dissolved solids upon saturation. Viscosities at 30 °C were uniformly lower than those measured at 20 °C, but the data at both temperatures followed nearly the same viscosity–sodium relationship. Hydroxide-only systems exhibited somewhat lower viscosities than carbonate-containing systems, whereas mixed carbonate–hydroxide matrices produced viscosities comparable to the carbonate-only regime.

Dissolved phosphate concentrations were also evaluated as a function of the measured final pH (Figure 1). Hydroxide-only systems exhibited higher pH than carbonate-containing solutions, and the corresponding increase in alkalinity was associated with lower trisodium phosphate dodecahydrate solubility. The pH values were measured at the equilibration temperature, and measurements collected at 30 °C were therefore obtained at 30 °C. In most cases, the measured pH at 30 °C was slightly higher than the corresponding values at 20 °C. An exception occurred in the NaOH-only system, where the measured pH did not follow the expected temperature trend. The data are retained for completeness but are not used in interpretation of the results due to their deviation from the overall behavior.

Free hydroxide equivalents increased approximately linearly with base loading across carbonate-only and mixed carbonate–hydroxide systems, with the mixed matrices exhibiting the highest alkalinity. Hydroxide-only systems exhibited comparatively lower values and showed limited variation after equilibration at 20 °C, where post-equilibration measurements clustered near approximately 1000 equivalents despite increasing NaOH concentration. In contrast, carbonate-containing systems exhibited a clearer dependence of alkalinity on base concentration, reflecting continued accumulation of dissolved species in solution.

Together, the linear density– and viscosity–sodium relationships indicate that bulk solution properties are dominated by total dissolved sodium rather than electrolyte identity. The modest property shifts accompanying equilibration therefore reflect incremental solute redistribution rather than structural changes in the solution. Having established that hydroxide-rich conditions drive phosphate-bearing systems into a constrained regime whereas carbonate-containing matrices sustain comparatively higher dissolved phosphate, carbonate loading was next evaluated in a chemically realistic 3.8 M sodium simulant. The objective of the following experiments was to quantify changes in dissolved sodium and bulk solution properties as Na_2CO_3 was introduced to saturation and to determine whether elevated carbonate loading destabilizes the existing phosphate inventory by inducing precipitation from the starting composition.

4.2 Natrophosphate Solubility in Solutions with Fixed Total Sodium Concentration (3.8 M)

4.2.1 Solution Phase Data

To determine the effect of electrolyte identity on phosphate solubility independently of sodium concentration, natrophosphate dissolution was measured under fixed total sodium conditions representative of tank supernatants (3.8 M total Na). Project Year 1 data demonstrated that electrolyte identity alters natrophosphate solubility. Phosphate was more soluble in mixed nitrate–carbonate solutions than in hydroxide-rich solutions at equivalent total sodium, and increasing sodium hydroxide concentration did not significantly change solubility.

Because total sodium was held constant, these observations indicated that phosphate behavior in concentrated alkaline systems cannot be explained solely by sodium concentration and required separation of sodium activity effects from electrolyte identity. In these tests, sodium nitrate ($NaNO_3$) was added to maintain the concentration of Na at ~3.8 M, and carbonate and hydroxide were added on a per-anion basis to isolate the effect of electrolyte identity on natrophosphate solubility.

Dissolved phosphorus concentrations were uniformly lower in ≥3.8 M Na solutions than in more dilute solutions (Figure 2), confirming that high-ionic-strength solutions suppress phosphate solubility. However, electrolyte identity produced distinct solubility responses under fixed total sodium. Increasing the fraction of Na_2CO_3 relative to $NaNO_3$ increased natrophosphate solubility, with dissolved phosphorus rising monotonically from approximately 0.05 to 0.08 M. In contrast, increasing NaOH under the same fixed-sodium conditions produced little systematic change in dissolved phosphorus, with concentrations remaining near approximately 0.05 M across the range examined. Dissolved fluoride concentrations decreased with increasing carbonate concentration and showed greater variability in hydroxide-rich systems, consistent with the noncongruent dissolution behavior discussed below. The measured sodium concentration in solution was predominantly clustered with the exception of a 1.2 M NaOH concentration, where an outlier included in the analysis for consistency shifted the mean and generated the large error bar.

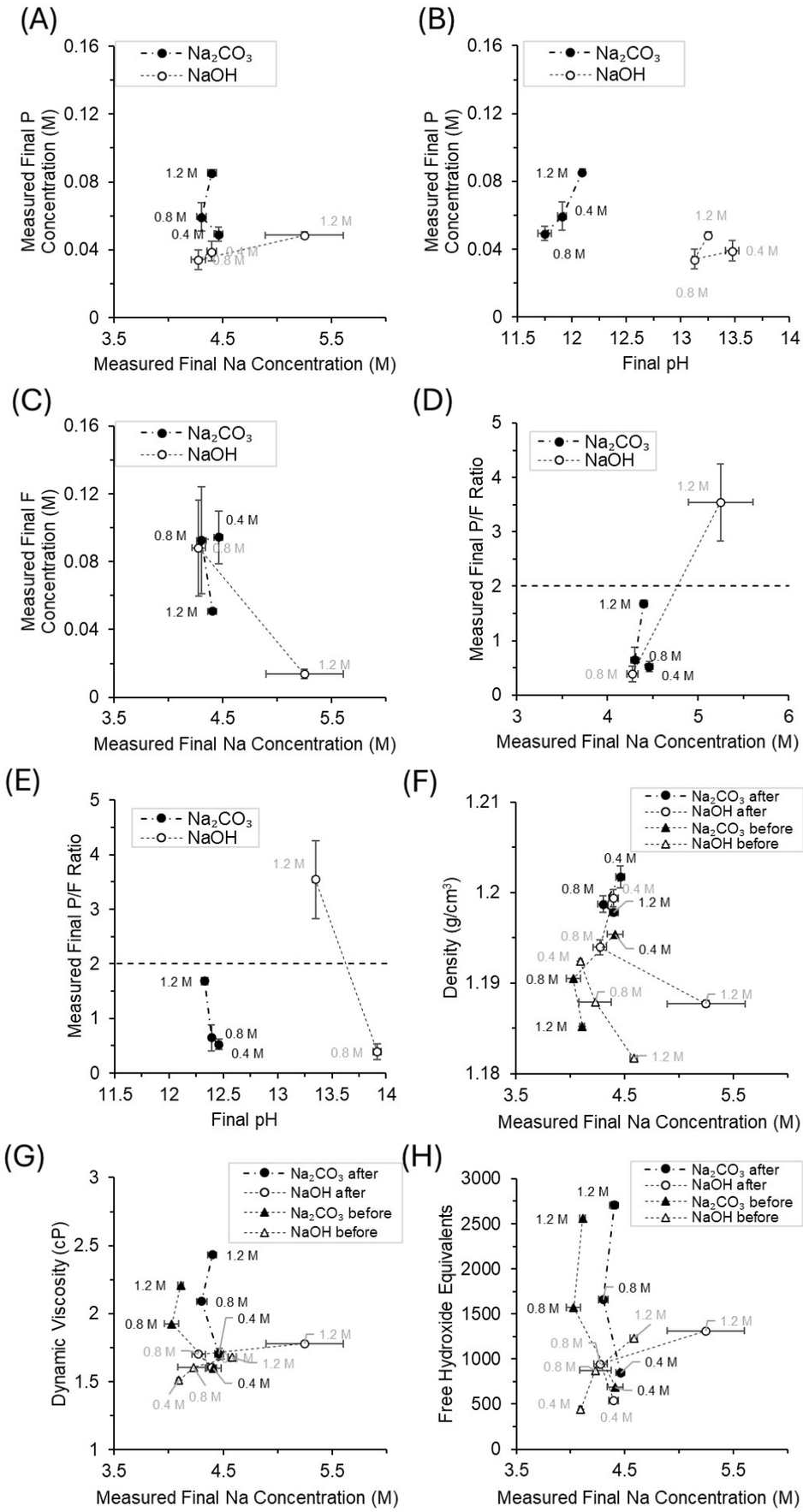

Figure 2. Natrophosphate equilibration behavior at 20 °C with the starting solution at a constant total Na concentration of ~3.8 M. (A) Final dissolved phosphorus concentration. (B) Final dissolved phosphorus concentration as a function of pH. (C) Final dissolved fluoride concentration. (D) P/F ratio as a function of final dissolved sodium where the dashed line indicates stoichiometric dissolution (P/F = 2) and (E) P/F ratio as a function of pH. (F) Density before and after equilibration. (G) Dynamic viscosity before and after equilibration. (H) Free hydroxide before and after equilibration.

Thus, although high ionic strength suppressed phosphate solubility, carbonate-containing solutions dissolved more phosphate than hydroxide-containing solutions at equivalent total sodium. The different extents of natrophosphate dissolution in carbonate solutions vs. hydroxide solutions indicates that alkalinity does not influence dissolution uniformly at fixed Na concentrations. Phosphate solubility was low in solutions containing hydroxide and did not change significantly as a function of hydroxide concentration. These results establish that carbonate has a significant effect on natrophosphate solubility at high ionic strength.

4.2.2 Solid Phase Characterization

Solids recovered after dissolution of natrophosphate were analyzed by X-ray powder diffraction (Table 7) to verify phase identity as a function of changing electrolyte compositions at ~3.8 M Na. Natrophosphate was the dominant crystalline phase, but peaks corresponding to trisodium phosphate hemihydrate ($Na_3PO_4 \cdot 10H_2O$) were present after exposure to solutions containing 1.2 M NaOH. The hemihydrate may have dehydrated from the dodecahydrate before analysis. Solids were separated without washing prior to drying; therefore, minor reflections corresponding to crystallization of residual solution phase salts (e.g., sodium nitrate and sodium carbonate monohydrate) were present and were not attributed to formation of independent equilibrium solid phases. These results indicate that, under high ionic strength conditions, the solubility controlling phosphate solid phase is only affected at high hydroxide concentrations and differences in phosphate solubility arise from solution-phase thermodynamic effects.

Table 7. Estimated weight fractions of solid phases that were separated from solutions with fixed concentration of 3.8 M Na, with natrophosphate in excess. Two samples contained unidentified peaks; the remaining phases are scaled to 100%. Empty cells are 0%. For Information Only.

Solution	Natrophosphate	$Na_3(PO_4) \cdot 0.5H_2O$	$Na_2CO_3 \cdot H_2O$	$NaNO_3$	Unknown
0.4 M Na_2CO_3 + 3 M $NaNO_3$	96%			4%	
0.8 M Na_2CO_3 + 2.2 M $NaNO_3$	96%			4%	
1.2 M Na_2CO_3 + 1.4 M $NaNO_3$	94%		4%	2%	
0.4 M NaOH + 3.4 M $NaNO_3$	96%			4%	Y
0.8 M NaOH + 3.0 M $NaNO_3$	92%			8%	
1.2 M NaOH + 2.6 M $NaNO_3$	68%	25%		7%	Y

4.2.3 Incongruent Natrophosphate Dissolution

As shown in Figure 2, in systems containing only natrophosphate as the source of dissolved phosphate and fluoride (Na_2CO_3, NaOH, and $NaNO_3$-adjusted formulations without added NaF or Na_3PO_4), the PO_4/F ratio is an indication of congruent vs. incongruent dissolution. Stoichiometric dissolution of natrophosphate would yield a molar PO_4/F ratio of 2:1 in solution. Deviations from this value therefore reflect electrolyte-controlled partitioning rather than contributions from secondary solid phases.

With the Na concentration held at 3.8 M through sodium nitrate addition, noncongruence persists but exhibits composition-dependent behavior. In carbonate-containing solutions, P/F ratios range from approximately 0.5 to 1.5 and increase systematically with increasing carbonate concentration. The P/F ratios deviate significantly from 2 in hydroxide-containing solutions and range from 0.5 to 3.5,

indicating that hydroxide suppresses PO_4 solubility relative to F more than carbonate. The PO_4/F ratios show little systematic dependence on NaOH concentration (Figure 2D–E).

Most systems exhibit ratios below the stoichiometric dissolution value of 2, indicating incongruent dissolution behavior. The system containing 1.2 M NaOH yielded a relatively low measured fluoride concentration, which increases the calculated P/F ratio and produces values slightly above the stoichiometric value. Incongruent dissolution of natrophosphate at 3.8 M Na indicates that ionic strength influences dissolution behavior, with the nature of the electrolyte governing the magnitude of phosphate–fluoride partitioning between the solution and solid phases.

4.2.4 Physicochemical Characterization

As shown in Figure 2, dynamic viscosity increased after equilibration relative to the initially prepared solutions with carbonate-containing solutions exhibiting slightly larger increases with concentration than hydroxide-containing solutions. Solution densities varied within a narrow range of approximately 1.18 to 1.21 g mL^{-1} and were slightly higher after equilibration. Density decreased slightly with increasing carbonate or hydroxide concentration, consistent with the fixed total sodium constraint, which limited changes in total dissolved solids.

Dissolved phosphate concentrations were also evaluated as a function of the measured final pH. Hydroxide-containing systems exhibited higher pH than carbonate-containing solutions under the fixed-sodium conditions, and the corresponding increase in alkalinity was associated with lower natrophosphate solubility. As expected, free hydroxide equivalents increased with increasing base concentration in both carbonate- and hydroxide-containing solutions (Figure 2). Carbonate-containing solutions exhibited substantially higher alkalinity, with free hydroxide equivalents approximately twice those measured in hydroxide-containing solutions. Natrophosphate dissolution increased alkalinity slightly, indicating small shifts in solution composition. Together, the limited viscosity and density changes and the systematic increase in free hydroxide equivalents confirm that the solutions remained within the intended fixed-sodium concentration and that the observed differences in phosphate solubility arise from electrolyte identity rather than large changes in bulk solution properties.

4.3 Natrophosphate Solubility in Solutions with Varying Na Concentration

Natrophosphate solubility was measured in solutions with varying Na concentrations to distinguish intrinsic carbonate and hydroxide effects from effects caused by addition of sodium nitrate.

4.3.1 Solution Phase Data

As shown in Figure 3, natrophosphate solubility changes as a function of carbonate, hydroxide, and sodium concentration. In Na_2CO_3 solutions, increasing carbonate concentration from 0.4 to 1.2 M decreased dissolved phosphorus slightly from 0.15 to 0.12 M. In NaOH solutions, dissolved phosphorous concentrations decreased monotonically over the same concentration range. Dissolved fluoride concentrations decreased with increasing base concentration in both carbonate- and hydroxide-containing solutions, and the decrease was greater with hydroxide. Na concentrations in solution increased as expected.

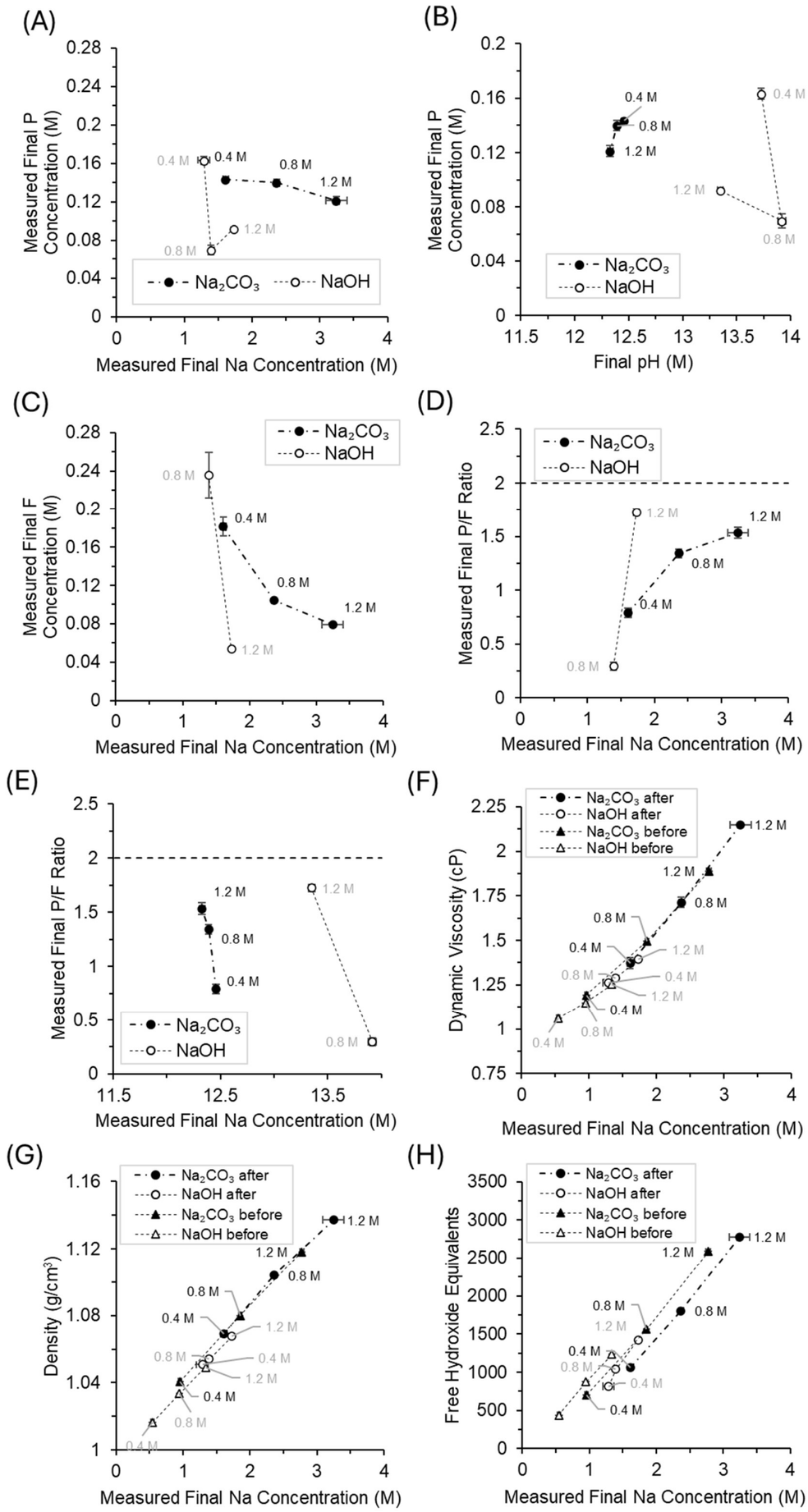

Figure 3. Natrophosphate equilibration behavior at 20 °C with varying Na concentration. (A) Final dissolved phosphorus concentration. (B) Final dissolved phosphorus concentration as a function of pH. (C) Final dissolved fluoride concentration. (D) P/F ratio as a function of final dissolved sodium where the dashed line indicates stoichiometric dissolution (P/F = 2) and (E) P/F ratio as a function of pH. (F) Dynamic viscosity before and after equilibration. (G) Density before and after equilibration. (H) Free hydroxide before and after equilibration.

4.3.2 Solid State Characterization

Solids recovered from variable-sodium systems were analyzed by X-ray powder diffraction to confirm solubility controlling phase identification in carbonate- and hydroxide-containing solutions (Table 8). Results were similar to those for fixed (3.8 M) Na concentration with natrophosphate the only phosphorus-bearing crystalline phase, except in solutions containing NaOH, in which an unknown phase precipitated, and at 1.2 M NaOH a solid Na_3PO_4 hydrate formed. Because solids were not washed prior to drying, trace amounts of salts precipitated from solution are present. Thus, changes in natrophosphate solubility are a result of solution-phase effects rather than changes in the solubility-controlling phase.

Table 8. Estimated weight fractions of solid phases separated from solutions with varying Na concentration, with natrophosphate in excess. Three samples contained unidentified peaks; the remaining phases are scaled to 100%. Empty cells are 0%. For Information Only.

Solution	Total Na (mol L-1)	Natrophosphate	$Na_3(PO_4)\cdot 0.5H_2O$	$Na_2CO_3\cdot H_2O$	Unknown
0.4 M Na_2CO_3	0.8	100%			
0.8 M Na_2CO_3	1.6	96%		4%	
1.2 M Na_2CO_3	2.4	97%		3%	
0.4 M NaOH	0.4	100%			Y
0.8 M NaOH	0.8	100%			Y
1.2 M NaOH	1.2	80%	20%		Y

4.3.3 Incongruent Natrophosphate Dissolution

The molar P/F ratio indicates congruent vs. incongruent dissolution in solutions where natrophosphate is the sole contributor of dissolved phosphate and fluoride (Na_2CO_3, NaOH, and $NaNO_3$-adjusted systems without added NaF or Na_3PO_4) (Figure 3**)**. A P/F ratio other than 2 in solution indicates electrolyte-dependent partitioning effects. In carbonate-containing solutions, P/F ratios range from 1 to 1.5, indicating persistent incongruent dissolution. In hydroxide-containing solutions, P/F ratios range from 0.5 to 2. The P/F ratios show little systematic dependence on pH. The data are approximately vertically aligned when plotted against pH, indicating that incongruent dissolution behavior is not strongly controlled by solution pH over the range examined. One data point associated with the 1.2 M NaOH system deviates from the general trend. The data are retained for completeness but are not used in interpretation of the results due to their deviation from the overall behavior.

4.3.4 Physicochemical Characterization

Dynamic viscosity and density increased with measured final sodium concentration across carbonate- and hydroxide-containing solutions (Figure 3). Dynamic viscosity increased systematically with increasing sodium concentration and was consistently higher after natrophosphate dissolution, reflecting the greater dissolved solids at saturation. When plotted as a function of final sodium concentration, viscosity values from carbonate- and hydroxide-containing solutions followed nearly the same trend, indicating that bulk rheological behavior was governed primarily by total dissolved sodium rather than electrolyte identity. Density also increased with sodium concentration and was higher after natrophosphate dissolution. As expected, free hydroxide equivalents increased with increasing Na_2CO_3 and NaOH concentration (Figure 3). Dissolved phosphate concentrations were also evaluated as a function of the measured final pH. As in the fixed-sodium systems, hydroxide-containing solutions exhibited higher pH values than carbonate-containing solutions, and the higher alkalinity corresponded to lower natrophosphate solubility.

Together, the viscosity, density, and hydroxide-equivalent measurements demonstrate that bulk solution properties are correlated with dissolved sodium and alkalinity rather than electrolyte identity, confirming that differences in phosphate solubility arise from solution thermodynamic effects rather than changes to bulk solution structure.

4.4 Carbonate Solubility in a 3.8 M Na Multicomponent Simulant

4.4.1 Solution Phase Data

Having established the carbonate–hydroxide suppression hierarchy in simplified electrolyte systems, the next step was to evaluate whether carbonate loading destabilizes the dissolved phosphate inventory in a chemically realistic multicomponent simulant representative of tank supernatants. The 3.8 M sodium simulant contained nitrate, nitrite, phosphate, fluoride, carbonate, and aluminate species at tank-relevant concentrations, introducing competing equilibria and potential secondary phase formation that were not present in simplified electrolyte matrices. Carbonate was therefore progressively added to the simulant and solution composition was monitored over time to determine both the extent of carbonate dissolution and whether delayed precipitation of phosphate-bearing phases occurs under high-ionic-strength conditions.

As shown in Figure 4, progressive carbonate addition increased total dissolved sodium from approximately 3 M to nearly 7 M, corresponding to dissolution of roughly 2 M Na_2CO_3 in the multicomponent matrix. Despite this substantial increase in sodium concentration, dissolved phosphate concentrations did not decrease systematically but instead fluctuated around a stable midpoint throughout the monitoring period. Fluoride concentrations exhibited similar small variations without sustained decline, while dissolved aluminum remained effectively constant. These observations indicate that elevated carbonate loading does not destabilize the dissolved phosphate inventory in the simulant, even as sodium concentrations increase substantially. Previous measurements in the same simulant showed that increasing NaOH concentration produces dose-dependent suppression of dissolved phosphate; together with the present carbonate-loading results, these observations demonstrate that the carbonate–hydroxide asymmetry identified in simplified electrolyte systems persists under realistic multicomponent conditions.

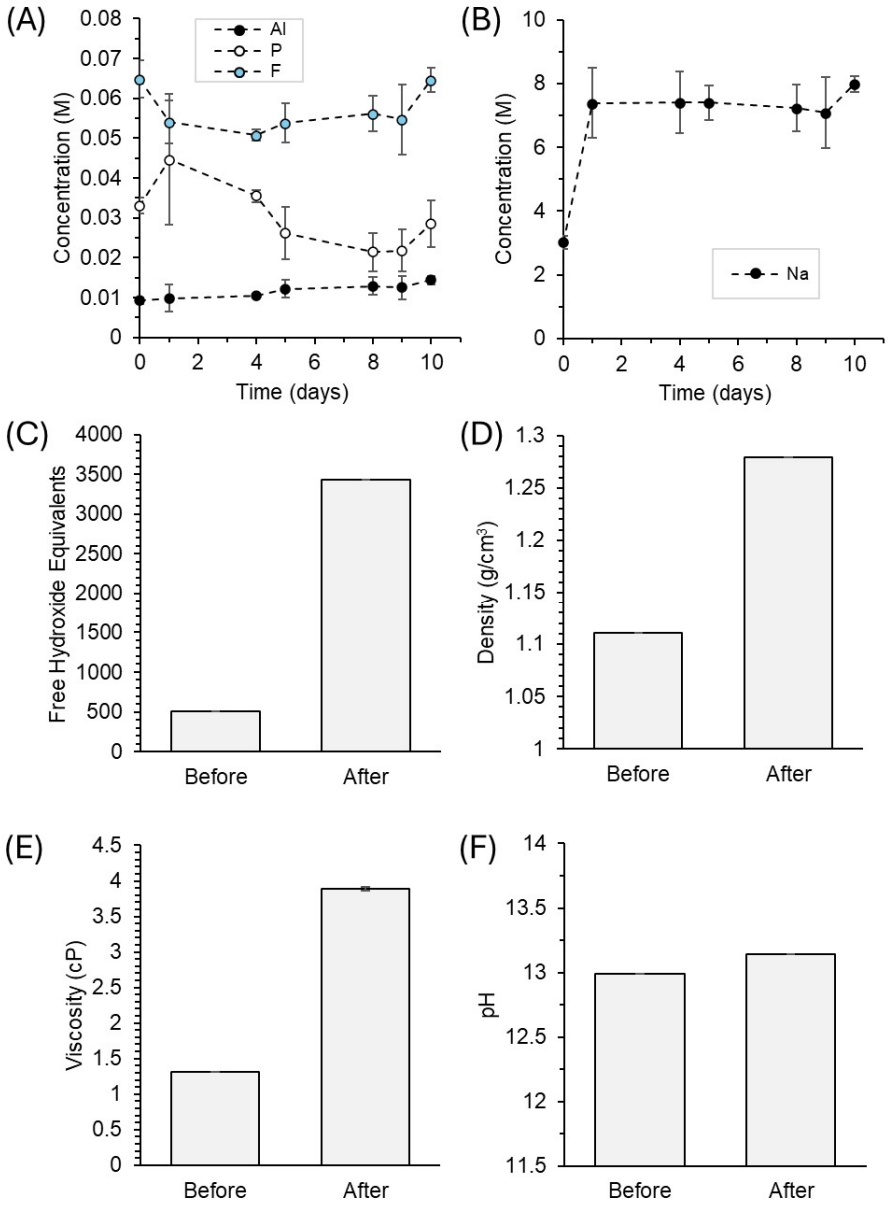

Figure 4. Dissolved (A) aluminum, phosphorus, and fluoride and (B) sodium in a 3.8 M multicomponent sodium simulant as a function of time during progressive carbonate loading. (C) Free hydroxide equivalents, (D) density, (E) viscosity, (F) pH.

4.4.2 Solid Phase Characterization

Solids recovered from the 3.8 M multicomponent simulant following progressive sodium carbonate loading were analyzed by X-ray powder diffraction to determine whether elevated carbonate concentrations induced formation of a phosphate-bearing crystalline phase. The recovered solid was dominated by sodium carbonate monohydrate, comprising approximately 93% of the crystalline material. Minor phases included natrophosphate (approximately 2%) and trace amounts of sodium nitrite and sodium nitrate (approximately 2% each). The predominance of sodium carbonate monohydrate reflects crystallization of carbonate under high loading conditions in the concentrated sodium matrix.

No bulk phosphorus-bearing crystalline phase was detected beyond the minor natrophosphate fraction. The small natrophosphate signal is attributed to entrained solid or residual material rather than to extensive precipitation induced by carbonate loading. The absence of a significant phosphate solid phase is consistent with the stable dissolved phosphate concentrations and indicates that elevated carbonate loading does not induce large-scale precipitation of a phosphate-bearing phase in the 3.8 M simulant. These results demonstrate that carbonate saturation in the multicomponent system leads primarily to carbonate crystallization without destabilizing the dissolved phosphate inventory under the conditions examined.

4.4.3 Physicochemical Characterization

Saturation of the 3.8 M multicomponent simulant with sodium carbonate (up to approximately 2 to 2.5 M additional Na_2CO_3) produced substantially larger changes in bulk solution properties than were observed in the simplified electrolyte systems. As carbonate loading approached saturation, solution density increased from approximately 1.1 g cm^{-3} to about 1.28 to 1.30 g cm^{-3}, reflecting the large increase in total dissolved solids. Dynamic viscosity increased from roughly 1.3 to 1.4 cP in the carbonate-free simulant to approximately 3.9 to 4 cP under carbonate-saturated conditions, representing an approximately threefold increase consistent with the elevated ionic strength and carbonate concentration in the high-sodium matrix. Free hydroxide equivalents increased from roughly 0.5 to approximately 3.5 over the same loading range, reflecting the increased alkalinity associated with carbonate dissolution.

Dissolved phosphate concentrations were also evaluated as a function of the measured final pH. Saturation with Na_2CO_3 produced little change in pH, with values remaining near approximately pH 13 across the carbonate-only systems. Despite these substantial changes in sodium concentration, density, viscosity, and alkalinity, dissolved phosphate concentrations remained within analytical uncertainty of their initial values throughout the monitoring period. Fluoride concentrations exhibited similar small variations without systematic decline, and no phosphate-bearing crystalline phase was detected. These observations demonstrate that elevated carbonate loading does not destabilize the dissolved phosphate inventory, even under conditions of markedly increased bulk solution density, viscosity, and alkalinity.

4.5 Phosphorus and Aluminum Solubility in Coupled Gibbsite–Natrophosphate Systems

While the experiments describe in the preceding sections examined equilibrium solubility under controlled electrolyte compositions, tank processing conditions can perturb alkalinity through dissolution of aluminum-bearing phases.

4.5.1 Solution Phase Studies

To assess the stability of phosphate-bearing systems under operationally relevant alkalinity perturbations, coupled natrophosphate–gibbsite experiments were conducted in the 3.8 M multicomponent simulant. Dissolution of gibbsite imposes a controlled hydroxide demand, redistributing alkalinity without external NaOH amendment and simulating conditions in which aluminum dissolution alters the hydroxide inventory. Time-dependent concentrations of dissolved aluminum, phosphate, and fluoride were monitored to determine whether phosphate remains stable as hydroxide is consumed within the high-sodium matrix. Systems containing nanoparticle and micro-scale gibbsite were examined to evaluate potential effects of particle size on dissolution behavior.

Figure 5 shows that dissolution of gibbsite in the absence of natrophosphate produces different steady-state aluminum concentrations for the two particle sizes, with nano-scale gibbsite yielding higher dissolved aluminum levels than micro-scale gibbsite. The simulant batches used for the nano- and micro-scale experiments exhibited slightly different initial pH values (approximately pH 12.7 and 12.5, respectively). This difference may have influenced the apparent aluminum solubility between the two systems. However, the effect cannot be separated conclusively from other batch-to-batch differences. Within each simulant batch, however, the pH values of experiments conducted with and without natrophosphate were equivalent. Consequently, comparisons between paired systems within each batch were not influenced by pH differences.

In the presence of excess natrophosphate, however, both nanoparticle and micro-scale gibbsite systems converged to similar steady-state aluminum concentrations. This convergence indicates that natrophosphate suppresses apparent gibbsite solubility under competitive conditions, effectively constraining the aluminum inventory to a common equilibrium level despite differences in particle size. Visual inspection of the time-dependent aluminum profiles suggests that micro-scale gibbsite dissolves more slowly when natrophosphate is present, although the available data are insufficient to determine whether a similar kinetic suppression occurs for nano-scale gibbsite.

In contrast to the evolving aluminum concentrations, dissolved phosphate and fluoride concentrations exhibited minimal variation over time in all systems examined. Phosphate levels remained stable despite ongoing gibbsite dissolution and associated hydroxide consumption, indicating that phosphate-bearing phases were not destabilized under the imposed perturbation. The rapid establishment of the phosphate inventory relative to the slower evolution of aluminum concentrations establishes a kinetic hierarchy in which natrophosphate dissolution equilibrates more quickly than gibbsite dissolution.

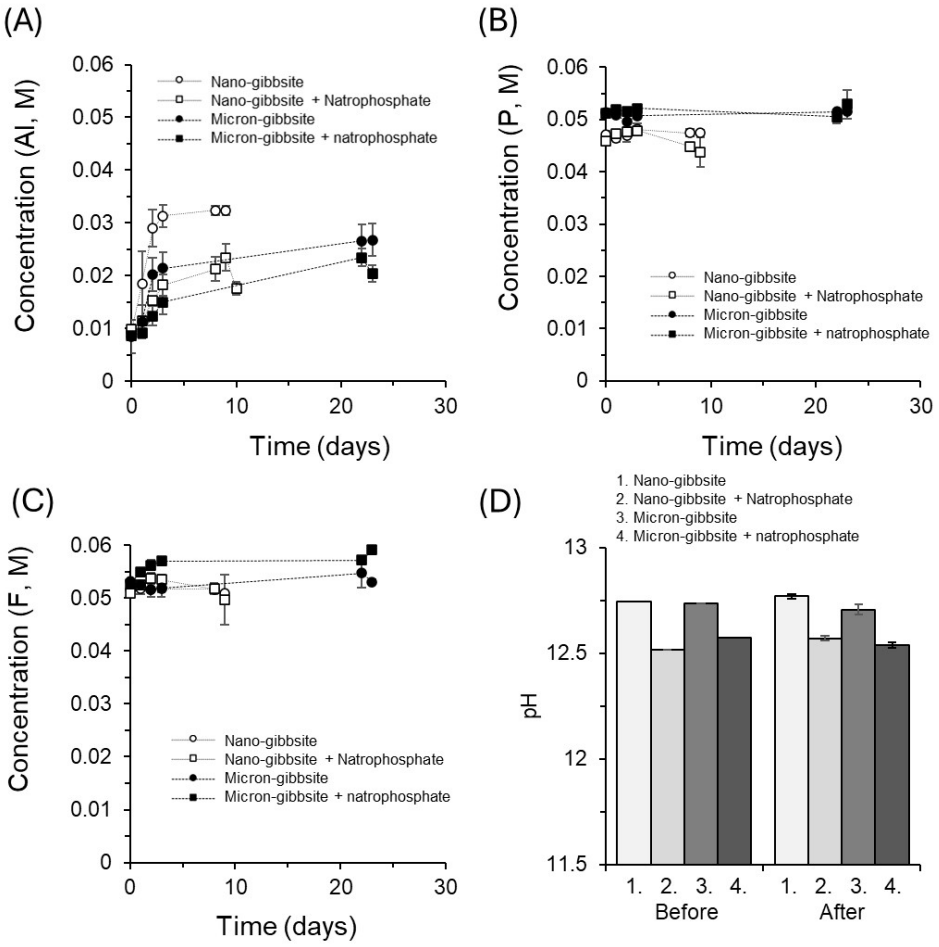

Figure 5. Dissolved (A) aluminum, (B) phosphorus, and (C) fluoride concentrations as a function of time for multicomponent simulant systems containing gibbsite alone and gibbsite in the presence of excess natrophosphate. (D) pH of the initial and final solutions after equilibration. Experiments were conducted with nano- and micro-scale gibbsite to evaluate particle-size effects on dissolution behavior. Phosphate and fluoride concentrations represent total dissolved concentrations including the initial solution composition.

4.5.2 Solid Phase Characterization

Solids recovered from coupled natrophosphate–gibbsite systems were analyzed to determine whether redistribution of alkalinity through aluminum dissolution induced formation of new phosphate-bearing phases (Table 9). Across all systems examined, the recovered solids were consistent with the initially introduced phases. Natrophosphate and gibbsite remained the dominant crystalline components, and no secondary phosphate phases were detected. Dissolution of gibbsite and associated consumption of hydroxide did not produce measurable decreases in dissolved phosphate or fluoride concentrations. The absence of new crystalline phosphate phases in the recovered solids is consistent with the stable dissolved-phase inventories observed during equilibration and following two-fold and four-fold dilution. These results indicate that redistribution of alkalinity through hydroxide consumption does not destabilize the dissolved phosphate inventory within the high-sodium matrix. The controlling phosphate solid phase remains unchanged, and the observed aluminum behavior reflects competitive dissolution and alkalinity partitioning rather than transformation of the phosphate solid phase.

Table 9. Estimated weight fractions of solid phases recovered from solubility experiments in simulant solutions with different added solids in excess. For Information Only

Excess Solid	Natrophosphate	Gibbsite	$Na_2CO_3 \cdot H_2O$	$NaNO_3$	$NaNO_2$
Natrophosphate	83%		6%	5%	6%
Gibbsite (400 nm)		75%	10%	7%	9%
Gibbsite (400 nm)		83%	8%	5%	4%
Gibbsite (10 μm)		93%	3%	2%	2%
Gibbsite (400 nm) & natrophosphate	76%	8%	7%	5%	4%
Gibbsite (10 μm) & natrophosphate	90%	10%			

4.5.3 Physicochemical Characterization

Redistribution of alkalinity through gibbsite dissolution in the presence of natrophosphate produced only minor changes in bulk solution properties. Dissolution of approximately 23.7 mM aluminum from nano-scale gibbsite in the presence of 0.65 M carbonate resulted in an average viscosity increase from 1.94 to 1.96 mPa·s (≈1.2%), consistent with the overall minor variation in bulk solution properties. The associated density change was negligible, from 1.1675 to 1.1681 g/cm³, representing an increase of approximately 0.04%. Comparable behavior was observed for systems containing micro-scale gibbsite, with viscosity increases of up to approximately 1%. Saturation of the carbonate-containing simulant with natrophosphate or gibbsite produced negligible changes in density within experimental uncertainty. Although gibbsite dissolution in the presence of natrophosphate was suppressed relative to gibbsite-only systems (17.6 mM Al dissolved for 400 nm particles), this suppression was not reflected in measurable density differences, which remained within analytical uncertainty.

The simulant batches used in the nano- and micro-scale gibbsite experiments exhibited slightly different initial pH values, approximately pH 12.7 for the nano-scale system and approximately pH 12.5 for the micro-scale system. This small difference in alkalinity contributes to the apparent difference in aluminum solubility observed between the two systems. However, within each simulant batch, the pH values for experiments conducted with and without excess natrophosphate were equivalent. Consequently, the trends observed between the paired systems within each batch cannot be attributed to differences in pH and instead reflect the influence of natrophosphate on gibbsite dissolution behavior.

Because these changes are small and exhibit no systematic trends beyond analytical variability, the results other than pH are summarized here rather than shown graphically. These modest changes in density and viscosity contrast sharply with the substantial viscosity increase observed during extreme carbonate loading, indicating that competitive dissolution and hydroxide redistribution do not induce large-scale restructuring of the bulk solution matrix.

4.5.4 Effect of Dilution on Phosphate and Aluminum Solubility

In addition to alkalinity redistribution, tank operations may introduce dilution through transfers or flush water additions. The coupled natrophosphate–gibbsite experiments establish the supernatant composition that results when a multicomponent simulant is conditioned by excess phosphate- and aluminum-bearing solids, redistributing alkalinity and defining a dissolved Al–P–F inventory. However, operational transients such as retrieval dilution, transfer flushes, or blending events perturb ionic strength and alkalinity without maintaining continuous contact with the original solids. To evaluate whether the conditioned supernatant is intrinsically stable to such perturbations, solids were separated after the competitive dissolution systems approached steady behavior and the clarified solutions were subjected to two-fold and four-fold dilution.

As shown in Figure 6, following two-fold and four-fold dilution of the clarified supernatant previously equilibrated with excess natrophosphate and gibbsite, dissolved aluminum, phosphate, and fluoride concentrations were monitored for 10 days. Minor scatter was observed in the analytical measurements, but no systematic temporal trends indicative of precipitation, additional dissolution, or progressive phase redistribution were detected. Dissolved aluminum concentrations remained within the range established prior to dilution, and dissolved phosphate and fluoride levels exhibited no consistent decline that would suggest secondary phase formation. Over the 10-day monitoring period and within the dilution factors examined, the conditioned supernatant remained compositionally stable, indicating that moderate dilution did not destabilize the dissolved aluminum or phosphate inventories under these baseline alkalinity conditions. As expected, dilution with water produced an immediate decrease in pH due to the reduction in alkalinity. After dilution, the measured pH remained stable over the monitoring period, indicating that no additional reactions occurred that measurably altered the hydroxide inventory of the solutions.

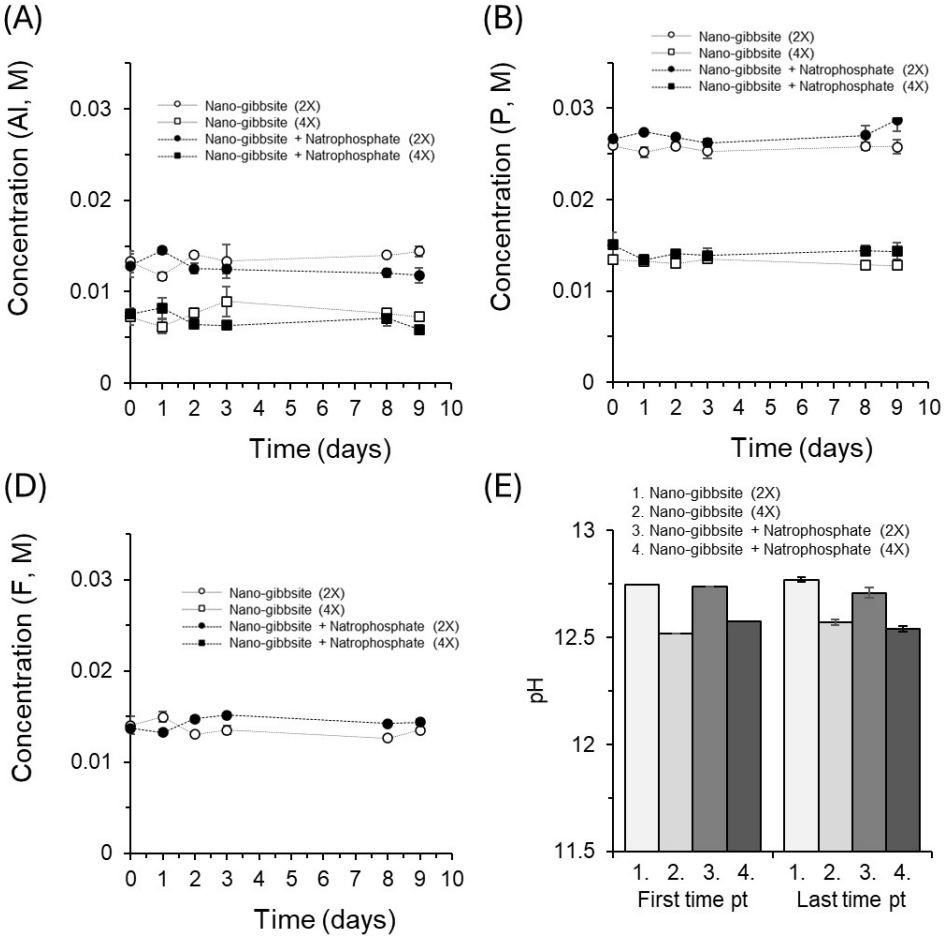

Figure 6. Dissolved (A) aluminum, (B) phosphorus, and (C) fluoride concentrations as a function of time following two-fold and four-fold dilution of clarified simulant solutions previously equilibrated with excess nanoparticle gibbsite, with and without excess natrophosphate. (D) pH of the solution immediately after dilution and the final time point (pt). Dilutions were performed after the systems approached steady behavior under the original high-ionic-strength matrix conditions.

5.0 Computational Chemistry Results

5.1 Development of a New Force Field for Alkaline Phosphate Solutions

While Year 1 was focused largely on the parameterization of new force fields for the simulation of trisodium phosphate in alkaline conditions, the validation of these force fields was extended into Year 2 to include the calculation of activity coefficients, comparison of inter-ion interactions with quantum mechanical *ab initio* molecular dynamics (AIMD) sampling, and solubilities. Year 1 had ended with the parameterized force fields (Madrid Transport, labeled MT, and the 2019 version of the Madrid force field, labeled M2019).

As illustrated in Figure 7, both models accurately capture the decreasing diffusion trends measured by PFG-NMR spectroscopy in Year 1. The underestimation of diffusivities of ^{31}P and ^{23}Na above 0.4 m suggests a slightly exaggerated aggregation behavior, which is also represented in hydrogen diffusivities. Almost all the hydrogen belongs to water in these simulations. The tendency of PO_4^{3-}–Na^+ contact ion pair formation promotes the growth of large ionic clusters, leaving the bulk water structure mostly unperturbed by ionic interactions. Thus, the calculated D_H remains closer to that of bulk water than experimentally observed. To explore the variation in the ion–ion interactions as a variable between the MT and M2019 force fields, AIMD potential of mean force simulations were performed to explore the Na_3PO_4 dimer potential energy diagram.

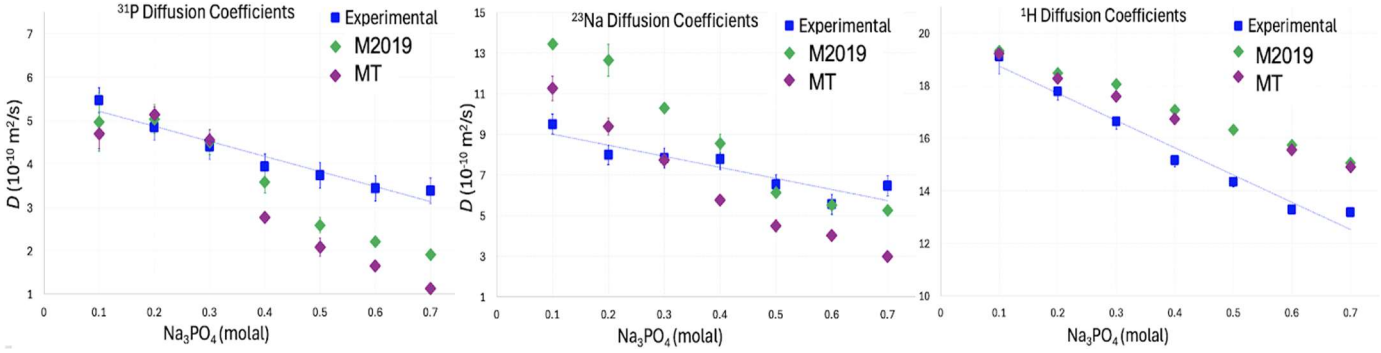

Figure 7. Concentration-dependent diffusivities of ^{31}P, ^{23}Na, and ^{1}H.

Both models reproduce the energy minimum predicted by AIMD simulation (Figure 8). Comparing the two methods, the sampling limitation of AIMD due to its high computational cost must be considered. Classical molecular dynamics is able to sample the positional fluctuations in both solvation shells, whereas AIMD is restricted to the positional fluctuations in the first solvation shell. The high energy barrier observed at ~6.5 Å in AIMD simulation is an artifact of this insufficient sampling.

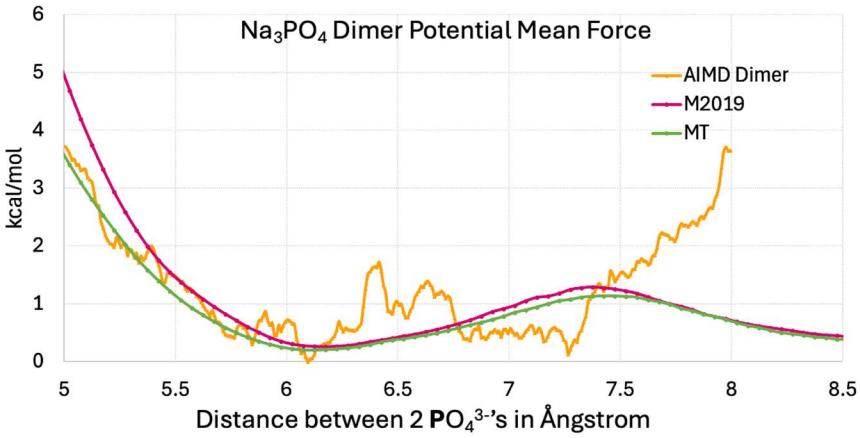

Figure 8. Potential of mean force diagram of Na_3PO_4 dimer. The x-axis is the distance between the two phosphorus atoms.

Another metric of the quality of the force fields is their ability to reproduce the water activity as a function of Na_3PO_4 concentration. Water activity in a solution of molality, m, depends on the excess chemical potential of water in that solution, $\mu_{w,m}^{ex}$, with respect to that in pure liquid water, $\mu_{w,m=0}^{ex}$ as given in Section 5.. First, the excess chemical potential of TIP4P/2005 water was calculated; the resulting value of −30.06 kJ/mol at 289 K is in good agreement with the reported literature value of −30.01 kJ/mol at 300 K (Rahbari et al. 2021). Concentration-dependent excess chemical potentials are given in Table 10. Both force fields exhibit the expected trend in the excess chemical potential of water, which decreases with increasing concentration of solution.

Table 10. Computed excess chemical potentials of water in aqueous sodium phosphate solutions.

Molality (m)	$\mu_{\text{M-2019}}^{\text{ex}}$ (kJ/mol)	$\mu_{\text{M-T}}^{\text{ex}}$ (kJ/mol)
0.0	-30.06	-30.06
0.3	-30.08	-30.09
0.5	-30.11	-30.10
0.6	-30.16	-30.15

The experimental activity of water in sodium phosphate solutions exhibits a very small decrease from 1 to 0.976 over the whole concentration range (0.0 to 0.7 m) (El Guendouzi and Benbiyi 2014). This narrow decrease in water activity is not surprising given the very low solubility (~0.7 m) of sodium phosphate. Strong ion-dipole interactions between the polar water and salt ions result in a decrease in the number of waters available to participate in physical processes like vaporization, and therefore a decrease in water activity, with increasing concentration of solutions. Both sets of force fields exhibit this behavior consistent with the experimental data (Figure 9). The water activities predicted by both force fields are in close agreement with the experimental activities.

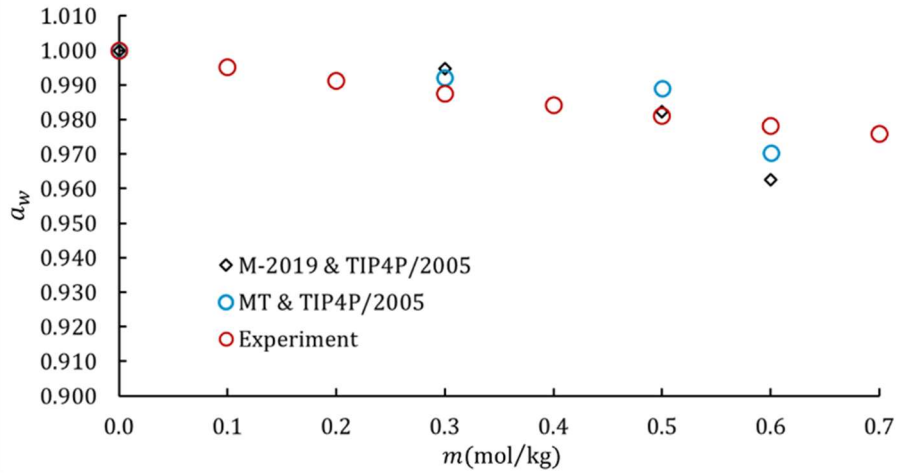

Figure 9. Water activity vs. the molality of aqueous sodium phosphate solutions at 298 K and 1 bar, for the M2019 and MT models. Red circles are experimental water activities (El Guendouzi and Benbiyi 2014).

Finally, we have begun direct solid-liquid coexistence simulations to assess the solubility that is predicted by the two force fields. These simulations are large (Figure 10) and take significant computational time to equilibrate the saturated trisodium phosphate solution concentration in contact with the different trisodium phosphate polymorphs. Specifically, we are calculating the solubility of Na_3PO_4 anhydrous and $Na_3PO_4 \cdot 12H_2O \cdot 1/6NaOH$, as detailed in Section 5.

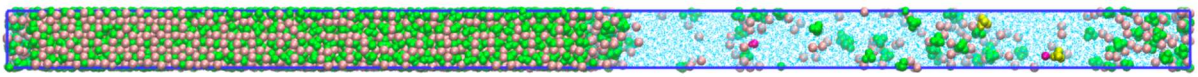

Figure 10. Equilibration of an anhydrous Na_3PO_4 crystal with its 0.5 m solution. In this representation: green, pink, magenta, and yellow vdW spheres represent PO_4^{3-}, Na^+, HPO_4^{2-}, and OH^- ions, respectively. Water is represented with cyan points.

The two newly parameterized alkali sodium phosphate solution force fields have now been validated against new experimental and AIMD data, relative to Year 1. Both models correctly predict the free-energy minima observed in AIMD-based Na_3PO_4 dimer potential of mean force calculations. The experimentally observed decreasing trend of the diffusivities is captured, though the models show a higher proneness to ionic aggregation. The thermodynamic prediction capabilities of the force fields are tested via water activity measurements, for which both force fields performed very well despite the narrow range of the experimental values. Initial results for the predicted solubilities look promising in that stable solid–solution interfaces are being obtained by the force fields and the specific solubility calculations are ongoing. These results establish that these models are adequate for studying the assembly pathways of these solutions.

5.2 Concentration-Dependent Aggregation Behavior of Na_3PO_4

Through visual inspection, it is easy to observe that the trisodium phosphate anions aggregate differently as a function of ion concentration. Coordination numbers derived from radial distribution function (Table 11) suggest that the amount of sodium in the first solvation shell of phosphates increases sharply with increasing concentration. This high number of sodium ions in the first solvation shell of phosphates at high concentrations suggests that the clustering behavior is dominated by contact ion pairs over solvent-separated waters characterized by ions that are bridged by a water molecule.

Table 11. Concentration-dependent PO_4^{3-} - Na^+ first shell coordination numbers.

Concentration (molal)	Coordination Number	
	MT	M2019
0.1	1.3	1.3
0.2	2.0	2.2
0.3	3.2	3.0
0.4	5.1	4.3
0.5	7.1	6.5
0.6	7.8	6.8
0.7	8.4	7.0

To confirm the contact ion pair formation in solution, a cluster size analysis was performed using molecular graph theory. The PO_4^{3-} and Na^+ ions were treated as nodes of a graph. A cutoff distance, determined by the location of the first well in the radial distribution function, was used to define PO_4^{3-}–Na^+ contact ion pair interaction. The results of this concentration-dependent analysis are presented in Figure 11. Results from both models point to the same clustering trends. At low concentrations, only small clusters of an exponentially decaying size distribution are present. Upon reaching a critical concentration, 0.4 m, this distribution separates into a bimodal distribution with a gaussian distribution for large-sized clusters.

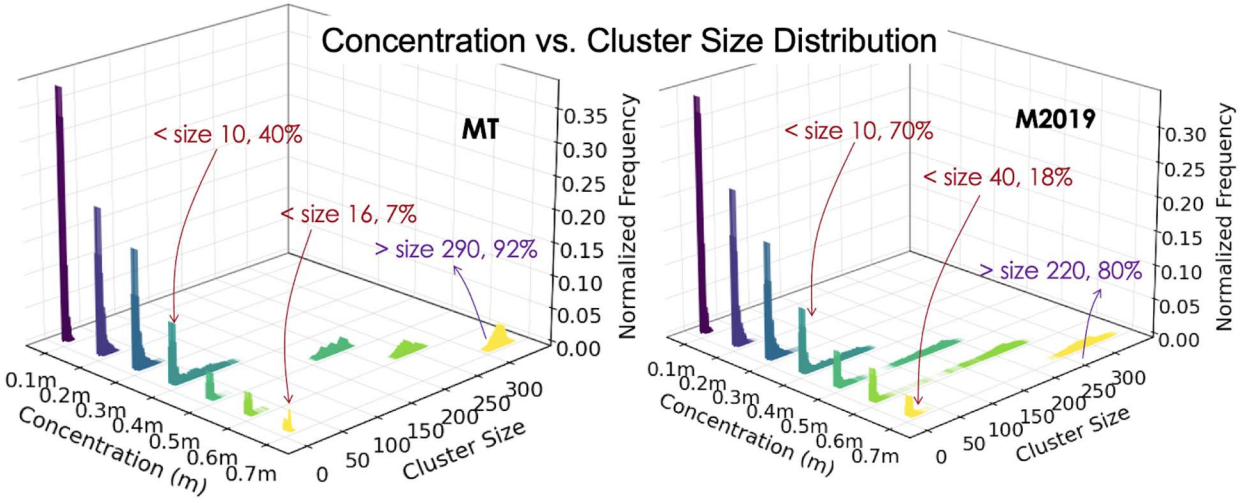

Figure 11. Concentration-dependent cluster size distribution of PO_4^{3-}–Na^+ contact ion pairs.

The stability of the clusters was examined by calculating the phosphate residence times, i.e., the time each phosphate spends in a given cluster size (Figure 12). These data indicate that the large clusters that form at higher concentrations are persistent throughout the simulations. This persistence can be attributed to the strong ionic interactions induced by the trivalent phosphate anion with the cation in solution, Na^+. Additionally, any “medium-sized” cluster that may form in solution is a transition between a small-sized cluster and a large-sized cluster and can be classified as a transient cluster.

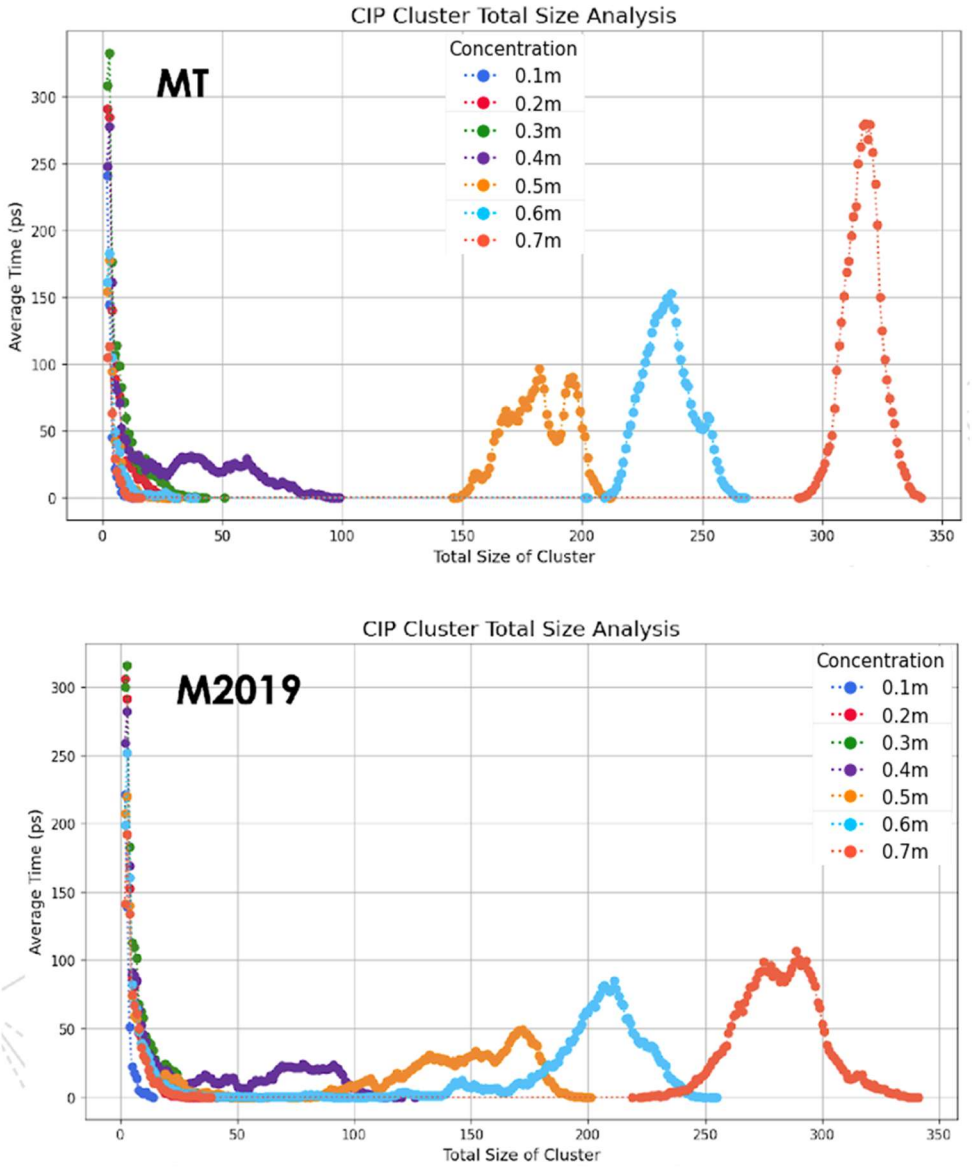

Figure 12. Residence time of PO_4^{3-} in solution clusters at different concentrations.

The persistence of the clusters means that the measured diffusivities of ^{23}Na and ^{31}P can be considered as the result of the ensemble average of the mixture of cluster distributions. Given the changes to the distribution, we approximate that at low concentration the diffusivities derive only from the small clusters, while at high concentrations the diffusivities result from a mixture. We implemented a simple binary mixture model to predict the diffusivity of the small clusters and large clusters. As shown in Table 12, the predicted diffusivity of the large clusters is 3 to 5× smaller than the small clusters observed at low concentration.

Table 12. D_P predicted in large clusters using a mixture model.

	MT	M2019
DP for low concentration (10-10 m2/s)	4.69 ± 0.34	4.96 ± 0.67
DP for high concentration (10-10 m2/s)	1.13 ± 0.07	1.91 ± 0.08
%population of large clusters to high conc.	93%	80%
Diffusion of large clusters (10-10 m2/s)	0.86	1.48

Given the success of the parameterized force fields in beginning to understand aggregation phenomena for trisodium phosphate-containing solutions, research has expanded to investigating the effects of competing anions on the assembly mechanisms. The F^-, NO_3^-, and CO_3^{2-} anions are of interest for their perturbation effects on the phosphate–sodium aggregate network. Initial studies with the M2019 force field for 0.1 m NaF added to 0.5 m Na_3PO_4 appear reasonable and show F^- competing with phosphate anions for sodium coordination (Figure 13).

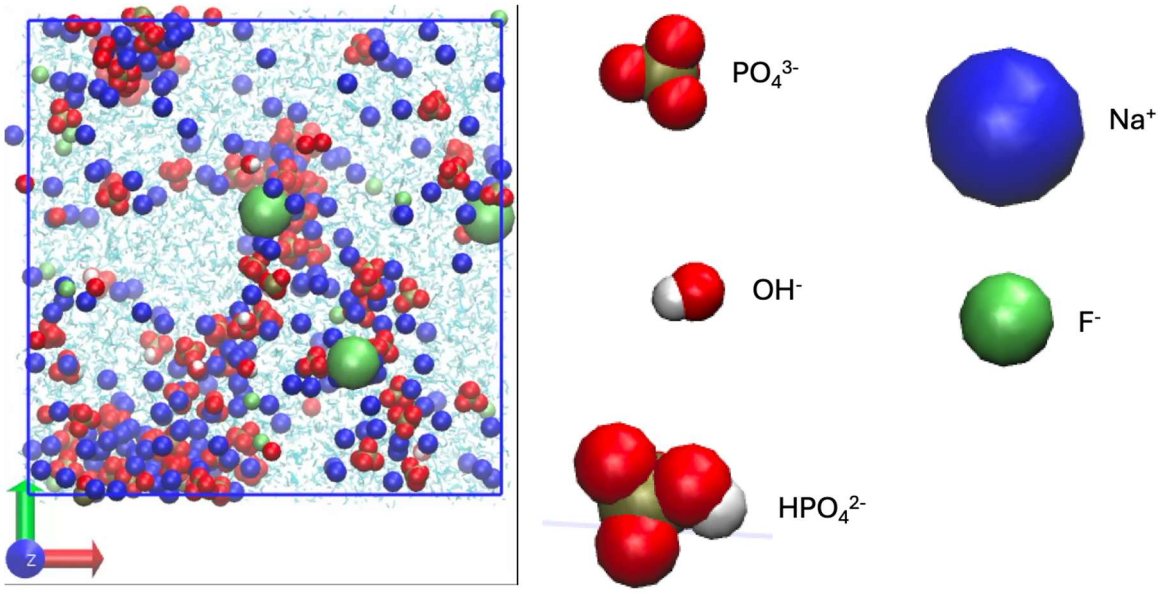

Figure 13. Snapshot from a simulation containing 216 Na^+, 59 PO_4^{3-}, 13 HPO_4^{2-}, 13 OH^-, and 20 NaF (using an unmodified M2019 force field for the description of fluoride).

As more experimental data become available, such as pH, pair distribution functions, and diffusion values of these systems, the fluoride model will be parameterized and validated further to match these data. In summary, as concentration increases, the contact ion pair-dominated Na_3PO_4 solution clusters grow in size. Upon reaching a critical concentration of 0.4 m, the clusters separate into two distinct populations of small clusters and large clusters. The large clusters, which persist throughout the simulation timescales, show a notable reduction in their diffusivity. Initial tests with other ions that are present in the tank show that the clustering mechanisms may be perturbed by the addition of anions that will compete to interact with sodium ions.

5.3 Solid-Liquid Interfacial Chemistry of Na_3PO_4 Polymorphs

The low solubility of different Na_3PO_4 crystals and the propensity for forming persistent large clusters raise the question of whether the observed solution aggregates can be classified as prenucleation clusters. To explore the similarities of solution clusters to ordered Na_3PO_4 solids, we needed to identify a suitable order parameter that can distinguish between the different polymorphs of the solids. Initial simulations of anhydrous Na_3PO_4 and $Na_3PO_4 \cdot 12H_2O \cdot 1/6NaOH$ solids were visually stable throughout the simulations performed at 293 K. Following this conclusion, a more in-depth analysis of stability was performed. The Steinhardt parameter distributions, as described in Section 5, of the single-frame experimental structures were compared to the simulated structure order parameter distributions.

Figure 14 shows the separated populations of PO_4^{3-} centers of the two crystals with $\overline{(q_4)}$ and $\overline{(q_6)}$ values. The Steinhardt parameter found to best distinguish the two structures is $\overline{(q_6)}$. For this bond order, Na_3PO_4 anhydrous has a higher value, ranging from 0.37 to 0.45, whereas the same value is quite low for the $Na_3PO_4 \cdot 12H_2O \cdot 1/6NaOH$ salt, ranging between 0.05 and 0.1.

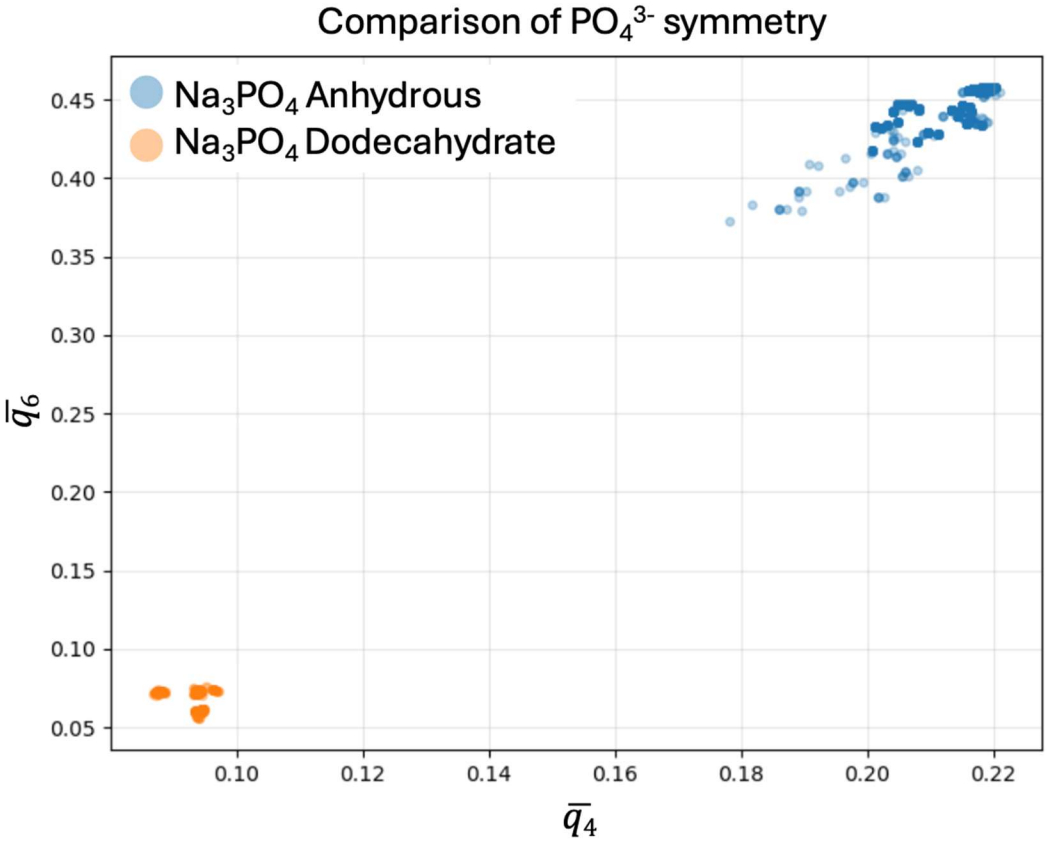

Figure 14. $\overline{q_4}$ and $\overline{q_6}$ value distribution of the phosphates in anhydrous and dodecahydrate polymorphs of trisodium dodecahydrate.

The ability to differentiate between different types of crystal structures is important for analyzing the large solution clusters and identifying their structures as solid-like or liquid-like. This information is now being extended to simulations where an interface along solid and liquid phases exists, namely for conclusively measuring equilibration of solubility simulations. Additionally, the disordered phases that form at the interface are being characterized using bond orders, starting with $\overline{q_6}$.

As illustrated in Figure 15, the extent and composition of this formed disordered layer depends on the identity of the solid phase. Ability to quantify the resemblance of solution clusters enables the identification of conditions that drive the formation clusters of one solid over the other.

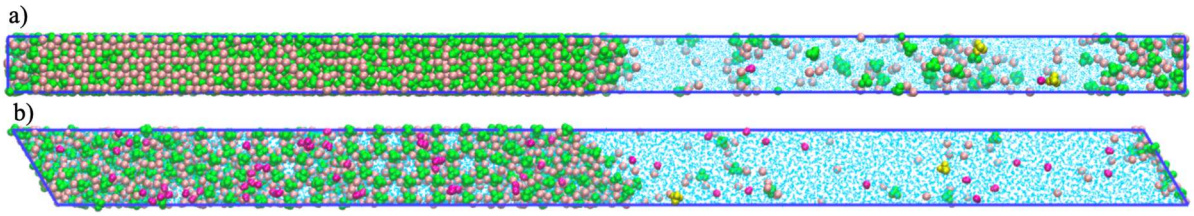

Figure 15. Representation of disordered interfaces of liquid and (a) Na_3PO_4 anhydrous and (b) $Na_3PO_4 \cdot 12H_2O \cdot 1/6NaOH$ crystals with the MT force field. Green, pink, magenta, and yellow vdW spheres represent PO_4^{3-}, Na^+, HPO_4^{2-}, and OH^- ions, respectively. Water is represented with cyan points.

6.0 Extension to Real Hanford Tank Waste

6.1 Aluminum Solubility

A post-leach solution was evaluated as a defined chemical state characterized by elevated hydroxide concentration, near 3.6 to 3.8 M total sodium, and minor concentrations of nitrate, nitrite, phosphate, and fluoride at 40 °C as shown in Table 13. To bound expected aluminum behavior under these conditions, equilibrium aluminum solubility was assessed using the NaOH-only gibbsite solubility based on regression of the data of Wesolowski (1992), which provides a conservative estimate of aluminum solubility as it does not take into account nanoparticle size and multicomponent electrolyte effects, which can increase the apparent solubility of aluminum in solution. The predicted equilibrium aluminum concentrations at 40 °C for 2.53 mol/kg of NaOH is 0.37 mol/kg Al, which is double the experimentally measured post-leach aluminum concentration as shown in Figure 16 establishing that the observed value lies below the equilibrium solubility envelope defined by both model-based and experimental constraints.

Table 13. Pre- and post-leach analytical results.

	Analyte	Pre-leach (M)	Post-leach (M)	Percent of Initial Solid Leached
Anions	Cl	0.024	0.023	-3%
	NO_2	0.244	0.231	-6%
	NO_3	0.184	0.178	-3%
	PO_4	0.010	0.009	-5%
	F	0.023	0.022	-3%
	SO_4	0.013	0.012	-5%
Titration	Free OH	2.53	2.62	3%
Metals / Non-metals	Al	0.020	0.196	90%
	Cr	[4.59E-04]	[4.37E-04]	-5%
	Na	3.86E+00	3.58E+00	-8%
	Zn	[2.17E-03]	[2.26E-03]	4%
	Cu	[2.26E-04]	[1.91E-04]	-19%
	Si	[2.97E-02]	[1.09E-02]	-172%

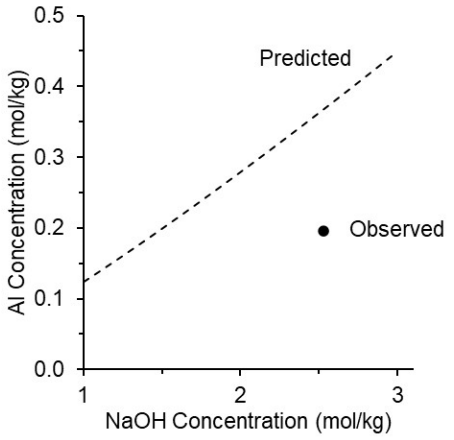

Figure 16. Predicted (line) aluminum concentration at 40 °C omitting enhancements arising from nanoparticle size and electrolytes beyond NaOH. The observed aluminum concentration (observed dot) is considerably below the expected Al concentration when solutions are saturated with gibbsite as the solubility-limiting phase.

Because the measured aluminum concentration is lower than equilibrium expectations under gibbsite control, the post-leach system is unlikely to be governed solely by gibbsite solubility. This offset is most plausibly attributed to control by less soluble aluminum-bearing phases (e.g., boehmite or mixed or poorly crystalline oxyhydroxides) and/or suppression of effective hydroxide activity due to contributions from non-hydroxide alkalinity (e.g., carbonate species). Under these conditions, dissolution of the gibbsite fraction is expected to proceed efficiently, while a residual fraction of aluminum remains associated with phases that are less reactive under the applied leach conditions. Accordingly, the observed post-leach aluminum concentration is chemically reasonable and is consistent with known aluminum solubility constraints rather than indicative of anomalous behavior or deficiencies in the underlying solubility framework.

6.2 Phosphate and Fluoride Solubility

Using the measurements of natrophosphate-associated total phosphate solubility as a reference, the Stage 1 fluoride concentration (0.029 M) can be evaluated indirectly through the coupled PO_4–F behavior of the natrophosphate phase. As summarized in the natrophosphate solubility dataset, total dissolved phosphate at 20 °C spans approximately 0.02 to 0.10 M across concentrated sodium matrices, with the lowest solubilities observed in strongly suppressing systems such as 3.8 M NaOH and progressively higher solubilities in nitrate-, nitrite-, carbonate-, and mixed-anion simulant systems. Because the Stage 1 matrix contains a higher total sodium concentration (~4.5 M Na) than the 3.8 M reference systems, suppression of natrophosphate dissolution relative to the nitrate/nitrite/simulant cases is expected. Accordingly, the observed Stage 1 fluoride concentration is consistent with natrophosphate control under a more strongly suppressing high-sodium matrix.

In contrast, the Stage 1 phosphate concentration (0.653 M) is far above the level that could be supplied by natrophosphate dissolution alone at this fluoride concentration. Stoichiometric natrophosphate dissolution would supply a maximum of 0.058 M phosphate (P/F = 2) at 0.029 M fluoride. The measured Stage 1 phosphate concentration of 0.653 M therefore exceeds natrophosphate-derived phosphate by approximately 0.595 M, confirming that the phosphate inventory is not controlled by natrophosphate equilibrium under these conditions.

Table 14. Stage 1 and Stage 3 dilution analytical.

	Analyte	Stage 1 Dilution (M)	Stage 3 Dilution (M)	Normalized Stage 3 Concentration (M)	Additional Solubility Ratio
Anions	Cl	0.019	0.015	0.045	2.394
	NO_2	0.384	0.128	0.376	0.979
	NO_3	0.130	0.054	0.159	1.224
	PO_4	0.653	0.278	0.819	1.254
	F	0.029	0.030	0.090	3.059
	SO_4	0.025	0.011	0.032	1.301
Titration	Free OH	<MDL	<MDL	--	--
Metals /Non-metals	Al	5.33E-03	2.72E-03	8.00E-03	1.50
	Cr	4.15E-03	1.47E-03	4.33E-03	1.04
	K	1.13E-02	6.80E-03	2.00E-02	1.76
	Na	4.50E+00	1.53E+00	4.50E+00	1.00
	U	1.80E-02	5.36E-03	1.58E-02	0.88
	Zn	2.20E-03	2.11E-03	6.22E-03	2.83
	Zr	8.01E-04	2.45E-04	7.20E-04	0.90

Trisodium phosphate dodecahydrate ($Na_3PO_4 \cdot 12H_2O$) was next evaluated as a potential controlling solid. In simple Na_3PO_4–H_2O systems, total phosphate solubility is strongly pH dependent, increasing from approximately 0.5 m at pH ~12.8 to ~0.7 m at pH ~12.2. In a separate titration experiment, saturated solutions prepared with anhydrous Na_3PO_4 had no detectable free hydroxide. In these solutions, the solubility was 0.7 m. However, this behavior does not transfer directly to the Stage 1 wash matrix, which is dominated by a high background sodium concentration rather than a single sodium phosphate salt. In concentrated sodium nitrate media (e.g., 3.8 M $NaNO_3$), reported total phosphate solubility associated with TSPD control is on the order of 0.1 M, reflecting strong common-ion and activity effects at high Na^+. Although the Stage 1 solution contains substantially lower nitrate and nitrite concentrations (~0.2 M combined), its total sodium concentration is higher (~4.5 M Na), such that sodium-driven suppression of sodium phosphate solubility remains a confounding factor.

7.0 Conclusions

This study demonstrates that phosphate solubility from dissolution of natrophosphate and trisodium phosphate dodecahydrate in concentrated alkaline sodium solutions is controlled not only by total sodium concentration but also by electrolyte identity. Under fixed 3.8 M sodium conditions, carbonate-containing solutions sustained higher concentrations of dissolved phosphate than hydroxide-containing solutions at equivalent total sodium, demonstrating that electrolyte identity alters phosphate solubility independently of sodium concentration.

The experimental results collectively demonstrate that phosphate solubility in concentrated alkaline sodium systems is governed by two interacting constraints. First, elevated sodium concentrations limit phosphate solubility. Second, at high sodium concentrations, electrolyte identity also influences phosphate solubility through changes in alkalinity as a function of hydroxide and carbonate concentration. Hydroxide reduces phosphate solubility more than carbonate in constant total sodium solutions. Hydroxide continues to have a greater effect than carbonate in multicomponent simulants relevant to tank waste processing.

With variable total sodium concentration, hydroxide limited the dissolution of natrophosphate more than carbonate at comparable base concentrations. Dissolution of trisodium phosphate dodecahydrate confirmed that trends in the reduction of phosphate solubility as a function of carbonate and hydroxide concentration are not influenced by co-dissolution of fluoride ions and are related to alkalinity partitioning behavior in phosphate systems. Sodium hydroxide limited trisodium phosphate dodecahydrate dissolution without proportionally increasing dissolved sodium, whereas sodium carbonate systems did not limit dissolution to the same extent.

In a multicomponent 3.8 M sodium simulant, increased carbonate concentration did not induce precipitation of dissolved phosphate, whereas increasing hydroxide reduced phosphate solubility in the same matrix. Consumption of hydroxide through aluminum dissolution did not affect phosphate solubility, and subsequent dilution over a 10-day period produced no measurable precipitation. These results indicate that phosphate-bearing solutions remain stable when hydroxide concentrations are reduced or diluted.

Complementary molecular simulations provide a mechanistic framework for interpreting experimental observations. Classical molecular dynamics simulations using the newly developed MT and M2019 force fields reproduce key thermodynamic and transport trends in trisodium phosphate solutions, including concentration-dependent diffusivities and water activities consistent with experimental measurements. Both models predict strong Na^{+}–PO_4^{3-} contact-ion pairing that increases with concentration, producing persistent sodium–phosphate clusters. Cluster size analysis reveals a transition near ~0.4 m Na_3PO_4 from small transient aggregates to a bimodal population containing large, long-lived clusters. These large clusters dominate transport behavior at higher concentrations and account for the reduced diffusivities observed experimentally.

The simulations further show that cluster growth arises from strong ion–ion interactions between trivalent phosphate anions and sodium cations, which promote formation of contact-ion-pair networks in concentrated alkaline solutions. Preliminary work shows that competitive anions such as fluoride may perturb this aggregation by competing for sodium coordination, providing a molecular explanation for the experimentally observed electrolyte-identity effects. Structural analysis using Steinhardt order parameters demonstrates that different trisodium phosphate polymorphs produce distinct solid–solution interfacial structures, suggesting that solution clusters may act as precursors to specific crystalline phases. Together, these computational results establish a molecular basis for the experimentally observed sodium–

phosphate coupling and electrolyte-dependent suppression behavior in concentrated alkaline sodium systems.

From an operational perspective, these results indicate that increased alkalinity due to carbonate addition is chemically compatible with phosphate-bearing supernatants under high-sodium conditions. Addition of carbonate does not induce precipitation of the dissolved phosphate, whereas addition of hydroxide reduces phosphate dissolution and solubility. Consumption of hydroxide through aluminum dissolution and hydroxide dilution through addition of water did not affect the concentration of phosphate in solution, demonstrating that phosphate-bearing solutions remain stable under realistic processing conditions.

8.0 References

Abascal, J. L. F., and C. Vega. 2005. "A general purpose model for the condensed phases of water: TIP4P/2005." *The Journal of Chemical Physics* 123 (23). https://doi.org/10.1063/1.2121687.

GROMACS 2024.3 Source code. Zenodo.

Bennett, C. H. 1976. "Efficient estimation of free energy differences from Monte Carlo data." *Journal of Computational Physics* 22 (2): 245–268. https://doi.org/https://doi.org/10.1016/0021-9991(76)90078-4.

Berendsen, H. J. C., J. P. M. Postma, W. F. van Gunsteren, A. DiNola, and J. R. Haak. 1984. "Molecular dynamics with coupling to an external bath." *The Journal of Chemical Physics* 81 (8): 3684–3690. https://doi.org/10.1063/1.448118.

Bernetti, M., and G. Bussi. 2020. "Pressure control using stochastic cell rescaling." *The Journal of Chemical Physics* 153 (11): 114107. https://doi.org/10.1063/5.0020514.

Blazquez, S., M. M. Conde, and C. Vega. 2023. "Scaled charges for ions: An improvement but not the final word for modeling electrolytes in water." *The Journal of Chemical Physics* 158 (5): 054505. https://doi.org/10.1063/5.0136498.

Britton, M. D. 2019a. *Analysis of GCALC Solubility Prediction Accuracy Between Rev 0 and Rev 2 Parameters.* Washington River Protection Solutions LLC, RPP-RPT-61498. Richland, WA.

Britton, M. D. 2019b. *Solubility Data Review* Washington River Protection Solutions LLC Richland, Washington.

Bussi, G., D. Donadio, and M. Parrinello. 2007. "Canonical sampling through velocity rescaling." *The Journal of Chemical Physics* 126 (1): 014101. https://doi.org/10.1063/1.2408420.

Colburn, H. A., and R. A. Peterson. 2021. "A history of Hanford tank waste, implications for waste treatment, and disposal." *Environmental Progress & Sustainable Energy* 40 (1): e13567. https://doi.org/https://doi.org/10.1002/ep.13567.

de Lucas, M., S. Blazquez, J. Troncoso, C. Vega, and F. Gámez. 2024. "Dressing a Nonpolarizable Force Field for OH– in TIP4P/2005 Aqueous Solutions with Corrected Hirshfeld Charges." *The Journal of Physical Chemistry Letters* 15 (37): 9411–9418. https://doi.org/10.1021/acs.jpclett.4c02261.

Dembowski, M., M. M. Snyder, C. H. Delegard, J. G. Reynolds, T. R. Graham, H.-W. Wang, I. I. Leavy, S. R. Baum, O. Qafoku, M. S. Fountain, K. M. Rosso, S. B. Clark, and C. I. Pearce. 2020. "Ion–ion interactions enhance aluminum solubility in alkaline suspensions of nano-gibbsite (α-Al(OH)3) with sodium nitrite/nitrate." *Physical Chemistry Chemical Physics* 22 (8): 4368–4378. https://doi.org/10.1039/C9CP05856G.

El Guendouzi, M., and A. Benbiyi. 2014. "Thermodynamic properties of binary aqueous solutions of orthophosphate salts, sodium, potassium and ammonium at T=298.15K." *Fluid Phase Equilibria* 369: 68–85. https://doi.org/https://doi.org/10.1016/j.fluid.2014.02.019.

Espinosa, J. R., J. M. Young, H. Jiang, D. Gupta, C. Vega, E. Sanz, P. G. Debenedetti, and A. Z. Panagiotopoulos. 2016. "On the calculation of solubilities via direct coexistence simulations:

Investigation of NaCl aqueous solutions and Lennard-Jones binary mixtures." *The Journal of Chemical Physics* 145 (15): 154111. https://doi.org/10.1063/1.4964725.

Graham, T. R., W. Liu, A. Ozkanlar, A. R. Kennedy, D. V. Boglaienko, X. Zhao, J. I. Morton, M. E. Bowden, T. L. Lemmon, M. S. Swita, H.-W. Wang, M. D. Britton, J. G. Reynolds, A. E. Clark, and C. I. Pearce. 2026. "Trisodium Phosphate Phases and Solubility in Alkaline Solutions Relevant to Radioactive Waste Processing." *Crystal Growth & Design* 26 (5): 2013–2022. https://doi.org/10.1021/acs.cgd.5c01598.

Graham, T. R., E. T. Nienhuis, J. G. Reynolds, J. Marcial, J. S. Loring, K. M. Rosso, and C. I. Pearce. 2022. "Sodium site occupancy and phosphate speciation in natrophosphate are invariant to changes in NaF and Na3PO4 concentration." *Inorganic Chemistry Frontiers* 9 (19): 4864–4875. https://doi.org/10.1039/D2QI00868H.

Habibi, P., H. M. Polat, S. Blazquez, C. Vega, P. Dey, T. J. H. Vlugt, and O. A. Moultos. 2024. "Accurate Free Energies of Aqueous Electrolyte Solutions from Molecular Simulations with Non-polarizable Force Fields." *The Journal of Physical Chemistry Letters* 15 (16): 4477–4485. https://doi.org/10.1021/acs.jpclett.4c00428.

Habibi, P., A. Rahbari, S. Blazquez, C. Vega, P. Dey, T. J. H. Vlugt, and O. A. Moultos. 2022. "A New Force Field for OH– for Computing Thermodynamic and Transport Properties of H2 and O2 in Aqueous NaOH and KOH Solutions." *The Journal of Physical Chemistry B* 126 (45): 9376–9387. https://doi.org/10.1021/acs.jpcb.2c06381.

Hempel, S., J. Fischer, D. Paschek, and G. Sadowski. 2012. "Activity Coefficients of Complex Molecules by Molecular Simulation and Gibbs-Duhem Integration." *Soft Materials* 10 (1-3): 26–41. https://doi.org/10.1080/1539445X.2011.599698.

Humphrey, W., A. Dalke, and K. Schulten. 1996. "VMD: Visual molecular dynamics." *Journal of Molecular Graphics* 14 (1): 33–38. https://doi.org/https://doi.org/10.1016/0263-7855(96)00018-5.

Lechner, W., and C. Dellago. 2008. "Accurate determination of crystal structures based on averaged local bond order parameters." *The Journal of Chemical Physics* 129 (11): 114707. https://doi.org/10.1063/1.2977970.

Martínez, L., R. Andrade, E. G. Birgin, and J. M. Martínez. 2009. "PACKMOL: A package for building initial configurations for molecular dynamics simulations." *Journal of Computational Chemistry* 30 (13): 2157–2164. https://doi.org/https://doi.org/10.1002/jcc.21224.

Miller, F. G., and M. D. Britton. 2017. *Analysis of GCALC Solubility Prediction Accuracy for Reference Data.* Washington River Protection Solutions Richland, WA.

Misra, C. 1970. "Solubility of aluminium trihydroxide (hydrargillite) in sodium hydroxide solutions." *Chemistry and Industry* 19 (5): 619–623.

Parrinello, M., and A. Rahman. 1981. "Polymorphic transitions in single crystals: A new molecular dynamics method." *Journal of Applied Physics* 52 (12): 7182–7190. https://doi.org/10.1063/1.328693.

Rahbari, A., J. C. Garcia-Navarro, M. Ramdin, L. J. P. van den Broeke, O. A. Moultos, D. Dubbeldam, and T. J. H. Vlugt. 2021. "Effect of Water Content on Thermodynamic Properties of Compressed

Hydrogen." *Journal of Chemical & Engineering Data* 66 (5): 2071–2087. https://doi.org/10.1021/acs.jced.1c00020.

Reynolds, J. G., D. R. Reinemann, M. S. Fountain, M. E. Stone, and R. B. Wyrwas. 2017. *One System River Protection Project Integrated Flowsheet Maturation Plan.* Washington River Protection Solutions, LLC Richland, Washington.

Steinbrecher, T., J. Latzer, and D. A. Case. 2012. "Revised AMBER Parameters for Bioorganic Phosphates." *Journal of Chemical Theory and Computation* 8 (11): 4405–4412. https://doi.org/10.1021/ct300613v.

Steinhardt, P. J., D. R. Nelson, and M. Ronchetti. 1983. "Bond-orientational order in liquids and glasses." *Physical Review B* 28 (2): 784–805. https://doi.org/10.1103/PhysRevB.28.784.

Wesolowski, D. J. 1992. "Aluminum speciation and equilibria in aqueous solution: I. The solubility of gibbsite in the system Na-K-Cl-OH-Al(OH)4 from 0 to 100°C." *Geochimica et Cosmochimica Acta* 56 (3): 1065–1091. https://doi.org/https://doi.org/10.1016/0016-7037(92)90047-M.

Zeron, I. M., J. L. F. Abascal, and C. Vega. 2019. "A force field of Li+, Na+, K+, Mg2+, Ca2+, Cl−, and SO42− in aqueous solution based on the TIP4P/2005 water model and scaled charges for the ions." *The Journal of Chemical Physics* 151 (13): 134504. https://doi.org/10.1063/1.5121392.

Zhang, X., X. Zhang, T. R. Graham, C. I. Pearce, B. L. Mehdi, A. T. N'Diaye, S. Kerisit, N. D. Browning, S. B. Clark, and K. M. Rosso. 2017. "Fast Synthesis of Gibbsite Nanoplates and Process Optimization using Box-Behnken Experimental Design." *Crystal Growth & Design* 17 (12): 6801–6808. https://doi.org/10.1021/acs.cgd.7b01400.

Zhu, C., L. Gong, and S.-n. Tie. 2020. "Influence of preparation processes on thermophysical properties of molten salt." *AIP Advances* 10 (2). https://doi.org/10.1063/1.5129609.

Pacific Northwest National Laboratory

902 Battelle Boulevard
P.O. Box 999
Richland, WA 99354

1-888-375-PNNL (7665)

www.pnnl.gov